Numerical MicroLocal Analysis Revisited

Jean-David Benamou, Francis Collino, Simon Marmorat

INSTITUT NATIONAL DE RECHERCHE EN INFORMATIQUE ET EN AUTOMATIQUE

Numerical MicroLocal Analysis Revisited

Jean-David Benamou — Francis Collino — SimonMarmorat

N° ????

Janvier 2011

Thème NUM

Rapport de recherche

ISSN 0249-6399 ISRN INRIA/RR--????--FR+ENG

INSTITUT NATIONAL DE RECHERCHE EN INFORMATIQUE ET EN AUTOMATIQUE

INRIA

centre de recherche PARIS - ROCQUENCOURT

Numerical MicroLocal Analysis Revisited

Jean-David Benamou*, Francis Collino† , SimonMarmorat‡

Thème NUM — Systèmes numériques
Équipes-Projets POEMS

Rapport de recherche n° ???? — Janvier 2011 — 59 pages

Abstract: The report bundles a theoretical and a numerical papier presenting a stable version of the NMLA algorithm as well a a new curvature estimation method and a linearization error correction method.

Key-words: Geometric Optics, Inverse Scattering, Asymptotic Analysis

* INRIA
† CERFACS
‡ INRIA

Centre de recherche INRIA Paris – Rocquencourt
Domaine de Voluceau, Rocquencourt, BP 105, 78153 Le Chesnay Cedex
Téléphone : +33 1 39 63 55 11 — Télécopie : +33 1 39 63 53 30

Nouvelle mouture pour l'Analyse MicroLocale Numérique

Résumé : Ce rapport rassemble un papier numérique et un papier théorique présentant une version stable de la méthode `NMLA` ainsi qu'une nouvelle méthode d'estimation de la courbure et une méthode de correction des erreurs de linéarisation.

Mots-clés : Optique géométrique, Scattering Inverse, Analyse Asymptotique

Numerical MicroLocal Analysis of 2-D Noisy Harmonic Plane Wave and Source Point Wavefields

J-D, Benamou[1] and F. Collino[2] S. Marmorat[1]

[1], INRIA, Domaine de Voluceau, Rocquencourt, France,

[2], CERFACS, 42 avenue G. Coriolis 31057, Toulouse, France,

E-mail: `Jean-david.Benamou@inria.fr`

Abstract. We present a mathematical and numerical analysis of the stability and accuracy of the `NMLA` (Numerical MicroLocal Analysis) method [3] and its discretization. We restrict to homogeneous space and focus on the two simplest field data cases : 1) Noisy plane wave packets, 2) Noisy point sources solution. A new stability result is obtained through the introduction of an impedant observable. The point source analysis leads to a modified second order (curvature Dependant) correction of the algorithm. As `NMLA` is local, it can be applied the second order improved version can be applied to general data (heterogeneous media). See [2] for a pedestrian description of the algorithm and an application to source discovery.

Keywords :plane waves, point source, inverse scattering

AMS classification scheme numbers: 78A05, 78A46, 78M35

1. Introduction

The use of a *formal high frequency asymptotic solution*‡ of the Helmholtz equation can be traced back to a 1911 paper of Debye on "the article of Sommerfeld", see [1]. It marked the beginning of the development of modern Geometric Optics numerical models and methods for the simulation of high frequency wave propagation which have been used in the industry for decades [5] [8].

In [3], we considered the inverse problem of numerically and locally extract the Geometric Optics components from harmonic wavefields. We also introduced a new approach named `NMLA` for Numerical MicroLocal Analysis to solve it. It is based a family of linear operators (or filters) B_k, indexed by the wavenumber k (see (4) for the new version of the filter). The filters are applied to observable harmonic wave data collected on a circle of fixed radius r_0 around an observation point x_0, in [3] we used the Dirichlet data :

$$U_k(\hat{s}) = u_k(x), \quad x = x_0 + r_0\hat{s}, \quad \hat{s} = (\cos\theta, \sin\theta). \tag{1}$$

When B_k is applied to an observable constructed from a finite number of plane waves :

$$u_k(x) = \sum_{p=1}^{P} b_p e^{-ik(x-x_0)\cdot\hat{s}_p}, \tag{2}$$

‡ also known as an Ansatz.

the output is an angular function presenting P picks of amplitude b_p at points localized approximatively at the $\hat{s}_p$'s. Both the localization of the picks and the quality of the evaluation of the amplitudes b_p increases with the frequency as we move in the high Frequency asymptotic regime, thus allowing in principle to estimate the number of high frequency wavefronts passing through x_0, their directions and amplitudes.

The stability of the original NMLA method was not clear and a L^2 Tychonov regularization was proposed in [3], see also [12] for a L^1 regularization. This paper introduces a new "impedant" observable and associated filters for which rigorous mathematical stability and localization error estimates are obtained in the case of noisy plane wave data. This is the topic of §2. In particular, Estimate (7) shows that the new "impedant filter" is very robust to noise.

The method however still relies on the plane wave assumption. General wave data will therefore carry linearization errors growing with the frequency which cannot be avoided. It can be rigorously analyzed on point source solution (§3.1). Ideally, second order terms should be identified and would allow to get a good approximation of the high frequency geometric optics amplitudes. It seems to be a quite difficult open problem. The closest related work that we know of, is the generalized Radon transform [4] which can be used to identify non linear patterns in images. This is not the philosophy of NMLA which uses the asymptotic geometric optics model (actually only the Eikonal equation so far) to reduce the complexity of the problem. As of today, we are still unable to incorporate the full second order term of the linearization in the identification process and use the transport equation for the geometric amplitudes.

So, we turned to the simplest solution of the Helmholtz equation after the plane wave, the above mentioned point source fundamental solution (in 2-D the Hankel function). Using classic FMM type asymptotic techniques [10], a second order correction can be analytically calculated (see §3) for the NMLA filters applied to a point source solution in homogeneous space. This is the simplest "constant curvature" non linear wave data. As we use this correction locally, it can be applied to general data, just assuming that instead of the the plane wave linearization we approximate the underlying high frequency solution by a constant curvature wavefront with an unknown virtual source. This correction to the classic NMLA filter is second order accurate, see [2] for a pedestrian presentation and numerical results.

§4 discusses the choice for the various discretization parameters of the NMLA filters.

§5 introduces an additional Gaussian filtering procedure which aims at removing interferences between plane waves when more that one. This is important in view of angular decomposition of the observable as the "constant curvature" correction of §3 only works when the wave data radiates from a single source.

A numerical illustration of these results is presented in §6.

2. Stable extraction of angles from noisy plane wave packets

2.1. A new impedant observable for `NMLA`

As discussed in the introduction, our new `NMLA` observable uses the impedant quantity on the same circle of radius r_0 centered at x_0 :

$$U_k(\hat{s}) = \left(\frac{1}{ik}\partial_{r_0} u_k(x) + u_k(x)\right), \quad x = x_0 + r_0\hat{s}, \quad \hat{s} = (\cos\theta, \sin\theta). \tag{3}$$

It is known that the knowledge of $U_k(\hat{s}) = U_k(\theta)$ and that u_k satisfies the Helmholtz equation inside the circle, is enough to reconstruct the whole solution since there is no resonance for an impedant Helmholtz problem : our observable contains hence all the information. As mentioned in the introduction, the observable in [3] was the restriction of u_k on the circle (compare with (1)). It does not allow to reconstruct the solution inside the circle for some exceptional values of k (Dirichlet resonance) and this deficiency underlies technical and practical important difficulties which are removed by (3).

Let us give the expression of the `NMLA` filters B_k for the new observable :

$$\begin{cases} B_k U(\theta) = \dfrac{1}{2L_k+1} \displaystyle\sum_{\ell=-L_k}^{L_k} \dfrac{(\mathcal{F}U)_\ell \; e^{i\ell\theta}}{(-i)^\ell (J_\ell(kr_0) - iJ'_\ell(kr_0))} \\ \quad \text{with } L_k = \max(1, [kr_0], \left[kr_0 + (kr_0)^{\frac{1}{3}} - 2.5\right]), \end{cases} \tag{4}$$

where $J_\ell(x)$ is the *Bessel functions of order ℓ and argument x*, $J'_\ell(x)$ their derivative and $(\mathcal{F}U)_\ell$ is the ℓ-th Fourier coefficient of U

$$(\mathcal{F}U)_\ell = \frac{1}{2\pi}\int_0^{2\pi} U(\theta) e^{-i\ell\theta}\, d\theta.$$

Note that the denominator in (4) never vanishes since $J_\ell(x)$ and $J'_\ell(x)$ have no common zeros (cf. Wronksian formula for Bessel Functions (A.2)).

2.2. Preliminary results for perturbed plane waves packets

We now assume noise perturbation of the plane wave data (2) :

$$U_k(\hat{s}) = U_k^{plane}(\hat{s}) + \delta U(\hat{s}). \tag{5}$$

The first term corresponds to the plane wave packets, the second one to the perturbation δu_k. The filters being linear we get

$$B_k U_k(\theta) = B_k U_k^{plane}(\theta) + B_k \delta U(\theta),$$

and as already noticed in [3] the part of U_k corresponding to the plane waves can be computed analytically; we have

$$B_k U_k^{plane}(\theta) = \sum_{p=1}^{P} b_p \psi_{L_k}(\theta - \theta_p),$$

where

$$\psi_L(\varphi) = \frac{\sin((L+\frac{1}{2})\varphi)}{(2L+1)\sin\frac{\varphi}{2}}.$$

The proof relies on *the Jacobi Anger Expansion*, [11, page 66]; we have

$$\left(\frac{1}{ik}\partial_{r_0}+1\right)(e^{-ikr_0\cos(\theta-\theta_p)})=\sum_{\ell=-\infty}^{\infty}\left(\frac{1}{ik}\partial_{r_0}+1\right)\left((-i)^{\ell}J_\ell(kr_0)e^{i\ell(\theta-\theta_p)}\right),$$

or

$$\left(\frac{1}{ik}\partial_{r_0}+1\right)(e^{-ikr_0\cos(\theta-\theta_p)})=\sum_{-\infty}^{\infty}(-i)^{\ell}\left(-iJ'_\ell(kr_0)+J_\ell(kr_0)\right)e^{i\ell(\theta-\theta_p)},$$

and, therefore,

$$B_k\left(\left(\frac{1}{ik}\partial_{r_0}+1\right)(e^{-ikr_0\cos(\theta-\theta_p)})\right)=\frac{1}{2L_k+1}\sum_{\ell=-L_k}^{L_k}e^{i\ell(\theta-\theta_p)}=\psi_{L_k}(\theta-\theta_p).$$

To understand how applying B_k to the observable provides a filtered output with picks localized at the angles of incidence, we use in the next section the properties of the function $\psi_L(\varphi)$ and a rather technical result that shows that one controls the norm of the operator B_k independently of the wavenumber k.

We start with function Ψ_L's properties :

(i) $\Psi_L(\varphi)$ is even; its maximum is reached at $\varphi=0$

$$\sup\Psi_L(\varphi)=1=\Psi_L(0).$$

(ii) $\Psi_L(\varphi)$ take values in the range of its maximum only in the vicinity of 0; we have

$$|\Psi_L(\varphi)|>0.45 \quad\Rightarrow\quad |\varphi|<\frac{2}{\sqrt{L(L+1)}}.$$

(iii) $\Psi_L(\varphi)$ is “small” far away from 0; we have

$$\Psi_L(\varphi)\le\frac{\pi}{2L+1}\frac{1}{|\varphi|}.$$

Concerning the bound on the norm of the B_k operators, we have the following result :

There exists a pure constant $B^\star$ (i.e. independent of k) such that

$$\sup_\theta|B_kU(\theta)|\le\frac{B^\star}{\sqrt{2\pi}}\|U\|_{L^2(0,2\pi)}\le B^\star\|U\|_{L^\infty(0,2\pi)}$$

This result strongly depends on the choice of the Fourier modes truncation level L_k in (4). Numerical experiments also shows that we have

$$B^\star\le 1,$$

and, even sharper

$$B^\star\le 0.89,$$

if we deal with high frequencies such that $kr_0>3$. These bounds on $B^\star$ mean that the filter operator does not amplify too much the noise.

The proof starts with Cauchy-Swartz

$$|B_kU(\theta)|\le\left[\frac{1}{2L_k+1}\left(\sum_{\ell=-L_k}^{L_k}\frac{1}{J_\ell^2(kr_0)+J_\ell'^2(kr_0)}\right)^{\frac12}\right]\left(\sum_{\ell=-\infty}^{\infty}|(\mathcal{F}U)_\ell|^2\right)^{\frac12},$$

then Parseval

$$|B_k U(\theta)| \leq \left[\frac{1}{2L_k+1}\left(\sum_{\ell=-L_k}^{L_k}\frac{1}{J_\ell^2(kr_0)+J_\ell'^2(kr_0)}\right)^{\frac{1}{2}}\right]\left(\frac{1}{2\pi}\int_0^{2\pi}|U(\varphi)|^2\,d\varphi\right)^{\frac{1}{2}}, \qquad (6)$$

and finally on a technical results (cf. appendix A) that shows that the term between hooks is bounded independently of k.

2.3. Confidence interval for angle extraction

Assuming $\theta^\star$ denotes the angle for which $\theta \mapsto |B_k U_k(\theta)|$ is maximum, we expect this will be the ray direction of the most energetic plane wave component. This section gives an error estimate on $\theta^\star$.

We begin with a single perturbed plane wave data :

$$B_k U_k(\theta) = b_1 \psi_{L_k}(\theta-\theta_1) + B_k \delta U.$$

Assume $|\theta-\theta_1| > \frac{2\pi}{2L_k+1}$, we use the third property of function Ψ_{L_k} and obtain

$$|B_k U_k(\theta)| \leq |b_1|\frac{\pi}{2L_k+1}\frac{2L_k+1}{2\pi} + B^\star\|\delta U\|_{L^\infty} \leq \frac{1}{2}|b_1| + B^\star\|\delta U\|_{L^\infty},$$

whereas, at $\theta=\theta_1$,

$$|B_k U_k(\theta_1)| \geq |b_1| - B^\star\|\delta U\|_{L^\infty}.$$

Thus, if perturbation due to the noise satisfies

$$2B^\star\|\delta U\|_{L^\infty} < \frac{1}{2}|b_1|, \qquad (7)$$

the maximum of $|B_k U_{plane}(\theta)|$ will be reached in a confidence interval centered around θ_1 with size $\frac{\pi}{L_k+\frac{1}{2}}$. When the frequency increases, since $L_k \sim kr_0$, the width of this interval will diminish and the angle of incidence is recovered with more precision. Remark that Inequality (7) is not very restrictive since a numerical estimate gives $\frac{1}{4B_\star} \simeq 0.28$: if the noise level does not overpass 28 % the angle will be detected within an interval of size $\sim \frac{2\pi}{k}$.

The general case of P plane waves is more technical, for simplicity we only detail the case $P=2$. We assume

$$B_k U_{plane}(\theta) = b_1 \Psi_{L_k}(\theta-\theta_1) + b_2 \Psi_{L_k}(\theta-\theta_2)\delta U, \text{ with } |b_2| < |b_1|.$$

We anticipate the maximum to be reached for $\theta \sim \theta_1$. At θ_1, we have

$$|B_k U_{plane}(\theta_1)| > |b_1| - \frac{\pi}{2L_k+1}\frac{1}{|\theta_2-\theta_1|} - B^\star\|\delta U\|_{L^2},$$

while for $\theta \in I = \left\{\theta,\, \max_{p=1,2}|\theta-\theta_p| > \frac{4\pi}{2L_k+1}\right\}$,

$$\begin{aligned}|B_k U_{plane}(\theta_)| &< \frac{\pi}{2L_k+1}\frac{2L_k+1}{4\pi}(|b_1|+|b_2|) + B^\star\|\delta U\|_{L^\infty} \\ &< \frac{1}{2}|b_1| + B^\star\|\delta U\|_{L^\infty}.\end{aligned}$$

The maximum is therefore be outside I if

$$2B^\star\|\delta U\|_{L^\infty} + \frac{\pi}{2L_k+1}\frac{|b_2|}{|\theta_2-\theta_1|} < \frac{1}{2}|b_1|.$$

A sufficient condition to ensure that the maximum is reached near θ_1, the angle of maximal amplitude, is

$$|b_2| + |b_1|\frac{\pi}{2L_k+1}\frac{1}{|\theta_1-\theta_2|} + 2B^\star\|\delta U\|_{L^\infty} \le |b_1|.$$

This inequality is asymptotically satisfied when the amplitude difference is not larger than the noise level. When $|b_1|$ is too close to $|b_2|$, the maximum may be erroneously located nearer to θ_2.

Let us point out that the width of the confidence interval I is twice larger than in the one plane wave case. This is a direct consequence of the possible interferences in the image by the `NMLA` filter of the two plane wave component if the angles are too close. Adding a Gaussian filter as proposed in §5 allows to consider treat well separated waves.

3. Source points identification using `NMLA`

3.1. Points sources viewed as local plane waves

After noisy plane wave packets (2), the simplest Helmholtz data are point sources solutions in homogeneous media. It also is the only other case we can handle analytically. So, we assume the data is generated from a P collection of source points x_p plus the now usual noise δu_k :

$$u_k(x) = \sum_{p=1}^{P} a_p\,\frac{i}{4} H_0^{(1)}(k|x-x_p|) + \delta u_k(x). \tag{8}$$

We have now $3\times P$ unknowns : the a_p's, θ_p's and R_p's, where

$$x_p = x_0 + R_p\hat{s}_p. = x_0 + R_p(\cos\theta_p, \sin\theta_p).$$

When the frequency goes to infinity, we can substitute to the Hankel function its asymptotic development, [11, page 65]

$$u_k(x) = \sum_{p=1}^{P} a_p\,\frac{e^{ik|x_p-x|}}{\sqrt{-ik\,8\pi|x_p-x|}} + \widetilde{\delta u}_k(x).$$

If we want to use `NMLA`, a natural idea is to linearize the data on the observation circle $x_0 + r_0\hat{s}$ around the observation point x_0 to find our usual plane wave packet. If r_0 is "small enough" with respect to all the R_p's, we will get have

$$u_k(x_0+r_0\hat{s}) = \sum_{p=1}^{P} b_p\, e^{-ikr_0\cos(\theta-\theta_p)} + \widetilde{\widetilde{\delta u}}_k(x), \text{ with } b_p = a_p\frac{e^{ikR_p}}{\sqrt{-ik\,8\pi R_p}}. \tag{9}$$

This means that, on the disk of center x_0 and radius r_0, the high frequency field is the sum of P plane waves plus some noise perturbation. The next step is to apply the previous filter (i.e. our operator B_k) to the impedant quantity (3). However, we need to be careful about the errors accumulated over the successive approximations (see the number of tildes rising over the perturbation term !).

If we just focus on the linearization error, we see that we used one term for the modulus and two terms for the phase in the expansion

$$\begin{aligned} k|x_p - x| \;&=\; k|x_p-x_0| - k(x-x_0)\cdot\hat{s}_p \\ &\quad + \frac{k}{2|x_p-x_0|}\left(|x-x_0|^2 - (x-x_0\cdot\hat{s}_p)^2\right) + \ldots, \end{aligned}$$

or, for $x = x_0 + r_0\hat{s}$

$$k|x_p - (x_0 + r_0\hat{s})| = kR_p - kr_0\cos(\theta - \theta_p) + \frac{kr_0^2}{2R_p}\sin^2(\theta - \theta_p) + \ldots \qquad (10)$$

For a fixed radius r_0, since the second order term goes to infinity with k, the `NMLA` filter is likely to fail. One would like to scale down the radius r_0 with the frequency to control it. However, we saw in §2 that stability and accuracy of the angle extraction depend on the truncation level L_k which is homogeneous to r_0. Somehow a finer analysis is needed.

3.2. Analysis of a `NMLA` *filtered source point*

We first assume that the data field corresponds to a unique source point

$$u_k(x) = a_1\frac{i}{4}H_0^{(1)}(k|x - x_1|) + \delta u_k(x).$$

Then, we use the *Graf addition Theorem*, [11, page 66]: when r_0 is smaller than $R_1 = |x_1 - x_0|$, we have

$$u_k(x_0 + r_0\hat{s}) = a_1\frac{i}{4}\sum_{\ell=-\infty}^{+\infty} H_\ell^{(1)}(kR_1)J_\ell(kr_0)\, e^{i\ell(\theta-\theta_1)} + \delta u_k(x_0 + r_0\hat{s}),$$

where θ (resp. θ_1) is the angle associated to $\hat{s}$ (resp. to $\frac{x_1-x_0}{|x_1-x_0|}$). The impedant quantity on the circle with the usual noise perturbation is

$$U_k(\theta) = U_k^{pt}(\theta) + \delta U_k(\theta),$$

where

$$\begin{aligned} U_k^{pt}(\theta) &= (\frac{1}{ik}\partial_{r_0} + 1)u_k(x_0 + r_0\hat{s}) \\ &= a_1\frac{i}{4}\sum_{\ell=-\infty}^{+\infty} H_\ell^{(1)}(kR_1)(J_\ell(kr_0) - iJ'_\ell(kr_0))\, e^{i\ell(\theta-\theta_1)}, \end{aligned}$$

or, after a change of variable

$$U_k^{pt}(\theta) = a_1\frac{e^{ikR_1}}{\sqrt{-ik\,8\pi R_1}}\sum_{\ell=-\infty}^{+\infty} C_\ell(kR_1)\,(-i)^\ell(J_\ell(kr_0) - iJ'_\ell(kr_0))\, e^{i\ell(\theta-\theta_1)},$$

with

$$C_\ell(kR_1) = i^\ell\sqrt{\frac{ik\pi R_1}{2}}\, e^{-ikR_1}\, H_\ell^{(1)}(kR_1). \qquad (11)$$

It is important to notice that when kR_1 is large enough $C_\ell(kR_1)$ is a perturbation of 1 due to the asymptotic, [13, page 198],

$$C_\ell(kR_1) \sim 1 + \sum_{m=1}^{\infty}\frac{(\ell, m)}{(-2ikR_1)^m}, \qquad (12)$$

$$\text{with } (\ell, m) = \frac{(4\ell^2 - 1^2)(4\ell^2 - 3^2)\ldots(4\ell^2 - (2m-1)^2)}{2^{2m}m!}.$$

The zeroth order approximation $C_\ell(kR_1) \sim 1$ corresponds to a plane wave linearization of the data. As in §2.2, the `NMLA` filter will map it to a the shape function $\Psi_{L_k}(\theta - \theta_1)$.

Consequently, we split the data between linear and remaining quantities and obtain (cf. definition of b_1 in (9) and the expression of the filter B_k in (4))

$$B_k U_k^{pt}(\theta) = b_1 \frac{1}{2L_k+1} \sum_{-L_k}^{L_k} C_\ell(kR_1)\, e^{i\ell(\theta-\theta_1)}, \tag{13}$$

or

$$B_k U_k^{pt}(\theta) = b_1 \Psi_{L_k}(\theta-\theta_1) + \delta\beta(\theta), \text{ where}$$

$$\delta\beta(\theta) = b_1 \frac{1}{2L_k+1} \sum_{-L_k}^{L_k} (C_\ell(kR_1)-1)\, e^{i\ell(\theta-\theta_1)}. \tag{14}$$

$\delta\beta$ is precisely the image of the linearization error by the filter. It can be bound as follows

$$|\delta\beta(\theta)| \le |b_1| \left(\frac{1}{2L_k+1} \sum_{\ell=-L_k}^{L_k} |C_\ell(kR_1)-1| \right) = |b_1|\, \mathcal{E}(L_k, kR_1).$$

We can then use the results of §2.3 , applying the filter to the impedant data linked to a unique noisy source point. The only change is the additional linearization noise :

$$B_k U_k(\theta) = b_1 \Psi_{L_k}(\theta-\theta_1) + \delta\beta(\theta) + B_k \delta U_k(\theta).$$

The supremum of this is function will correspond to an angle located at a distance less than $\frac{\pi}{L_k+\frac{1}{2}}$ of θ_1, as soon as

$$\frac{2B^\star}{|b_1|} \|\delta U\|_{L^\infty} + \mathcal{E}(L_k, kR_1) \le \frac{1}{2}.$$

To go further, we need an estimate of the perturbation; it can be done numerically; for $\mathcal{E}(L_k, kR_1)$ bounded by, let say $\epsilon = 10^{-1}$, 10^{-2} or 10^{-3}, numerical computations show that the L_k parameter must approximately satisfy the respective inequalities (with some approximations)

$$L_k \le C_\epsilon \sqrt{kR_1} \quad \text{with } C_{0.1} = 0.775,\ C_{0.1} = 0.25 \quad C_{0.001} = 0.0775. \tag{15}$$

The $\sqrt{kR_1}$ dependency is not surprising when we look at the second order term neglected in the Taylor development of the phase (10).

Note that Inequality (15) is not unconditionally satisfied when L_k $(= [kr_0 + (kr_0)^{\frac{1}{3}} - 2.5])$ grows and k is too large (as discussed in §3.1). To fix the problem one may try to chose the radius of the circle r_0 such that

$$kr_0 + (kr_0)^{\frac{1}{3}} - 1.5 \le C_\epsilon (kR_1)^{\frac{1}{2}}.$$

Asymptotically r_0 must go to 0 like

$$r_0 \sim \frac{1}{4}\sqrt{\frac{R_1}{k}}$$

(we chose $\epsilon = 10^{-2}$ to simplify). As R_1 is unknown, this formula is not practical, but we can replace R_1 by any estimate from below of this distance. More important, picking a radius which decreases like the square root of the wavenumber will induce a decrease of L_k and, consequently, of the localization of the pick, i.e. of the angle of incidence.

In §3.3, we use more terms in the asymptotic series (12) to correct the `NMLA` filter up to second order.

3.3. Second order correction of the filter for a source point

We saw in the previous sections that the good angle localization property obtained for noisy plane wave data does not carry to point source data. We also know that the linearization is responsible for this loss of accuracy. Roughly speaking, the localization is in $\frac{C}{k}$ for a plane wave and $\frac{C'}{\sqrt{k}}$ for the source point. This section shows that it is possible to identify the curvature from the filtered image of the observable and then use it to improve the angle extraction.

We forget about the noise for now and apply `NMLA` to the impedant data associated to a source point. We then get (using the maximum test) a first estimate of the true angle $\theta_1 = \frac{x_1 - x_0}{|x_1 - x_0|}$; this first estimation is denoted θ_{est}. The Fourier coefficients $\hat{\beta}_\ell$ of $B_k U_k^{pt}(\theta)$ are analytically given by (cf. Formula (13))

$$\hat{\beta}_\ell = \frac{1}{2L_k+1} C_\ell(kR_1)\, e^{-i\ell\theta_1}.$$

We shift the phase for convenience :

$$\hat{\beta}_\ell e^{i\ell\theta_{est}} = \frac{1}{2L_k+1} C_\ell(kR_1)\, e^{i\ell(\theta_{est}-\theta_1)} = \frac{1}{2L_k+1} C_\ell(kR_1)\, e^{i\ell\delta\theta},$$

where $\delta\theta = \theta_{est} - \theta_1$ is the error we make on the angle. We now use a second order asymptotic from (12),

$$C_\ell(kR_1) \simeq \frac{e^{i\frac{\ell^2-\frac{1}{4}}{2kR_1}}}{\left(1 - \frac{\ell^2-\frac{1}{4}}{(kR_1)^2}\right)^{\frac{1}{4}}}, \tag{16}$$

and obtain

$$\hat{\beta}_\ell e^{i\ell\theta_{est}} = \frac{1}{2L_k+1} e^{i\left(\ell\delta\theta + \frac{\ell^2-\frac{1}{4}}{2kR_1}\right)} \frac{1}{\left(1 - \frac{\ell^2-\frac{1}{4}}{(kR_1)^2}\right)^{\frac{1}{4}}} + O(\frac{1}{(kR_1)^3}).$$

If we consider($\Im$ stands for imaginary part)

$$\varphi_\ell = \Im\left(\log(\hat{\beta}_\ell e^{i\ell\theta_{est}}) - \log(\hat{\beta}_0)\right) \simeq \ell\delta\theta + \frac{\ell^2}{2kR_1}, \tag{17}$$

we see that we get a parabolic drift of the phase. The correction process consists in computing the closest parabola (for instance in the least square sense) of $\ell \mapsto \varphi_\ell$ for $|\ell| \leq L_k$. A weighted optimization can be used to take into account that the asymptotic is more accurate for small ℓs. The estimated parabola coefficients $\delta\theta_{est}$ and R_{est} provide a correction on the angle and an estimation of the distance to the source or equivalently of the front curvature.

These, in turn can be used to construct a corrected filter :

$$B_k^{cor} U(\theta) = \frac{1}{2L_k+1} \sum_{\ell=-L_k}^{L_k} \frac{(\mathcal{F}U)_\ell\, e^{i\ell\theta} \hat{C}_\ell^{cor}}{(-i)^\ell (J_\ell(kr_0) - iJ'_\ell(kr_0))} \tag{18}$$

$$\text{with } \hat{C}_\ell^{cor} = e^{-i\ell\left(\delta\theta_{est} + \frac{\ell^2-\frac{1}{4}}{2kR_{est}}\right)} \left(1 - \frac{\ell^2 - \frac{1}{4}}{(kR_{est})^2}\right)^{\frac{1}{4}},$$

which gives better localization as the parabolic drift of the phase of $\hat{\beta}_\ell$ has been removed. Remark that $\left|\hat{C}_\ell^{cor}\right| \leq 1$, and so the uniform stability estimate in k of the norm of B_k (7) also holds for B_k^{cor}: $\|B_k^{cor}\| \leq B_\star$ independent of k.

This modified corrected filter will yield a better result only if the error induced by approximation (16) is small enough to not perturb too much the value of the maximum. Using the approach described in the previous section, we have to make sure that

$$\mathcal{E}'(kR_1, L_k) = \left(\frac{1}{2L_k+1} \sum_{\ell=-L_k}^{L_k} \left| C_\ell(kR_1) - \frac{e^{i\frac{\ell^2-\frac{1}{4}}{2kR_1}}}{\left(1 - \frac{\ell^2-\frac{1}{4}}{(kR_1)^2}\right)^{\frac{1}{4}}} \right| \right) \leq \epsilon, \tag{19}$$

where we used the truncation, now up to second order, of the asymptotic series (12). Again, we performed numerical computations which show that when $kR_1 > 4.25$ then (19) is satisfied when $L_k + 1 \leq C_\epsilon (kR_1)^{\frac{3}{4}}$, with $C_\epsilon = 1.75$, 1.05, 0.59, for ϵ equals to 10^{-1}, 10^{-2}, 10^{-3}. Corrected `NMLA` will only succeed if

$$kr_0 + (kr_0)^{\frac{1}{3}} \leq C_\epsilon (kR_1)^{\frac{3}{4}}.$$

The radius r_0 must asymptotically behave like

$$r_0 \sim C_\epsilon \frac{R_1^{\frac{3}{4}}}{k^{\frac{1}{4}}}.$$

The confidence interval $\frac{\pi}{L_k+\frac{1}{2}}$ for angle localization (see §3.2) is improved and vary now like $\frac{C}{k^{\frac{3}{4}}}$.

4. Discretization parameters

We discuss here the discretization of the process. In [3], we proposed to discretize the observable as well as its filtered image by B_k using the same $2L_k + 1$ number of equidistributed samples. In other words, the number of Fourier coefficients of the filter was linked to the discretization. In practice though, we are free to use different numbers. We therefore relax this constraint and discuss here the choice of these parameters. The observable will be sampled with $P > 2L_k + 1$ points while its filtered image will be sampled in $Q > 2L_k + 1$ points.

We show that number P must be chosen large enough for the L_k Fourier coefficients to be correctly evaluated, while the number Q must be large enough to capture with sufficient precision the angle corresponding to the maximum of the modulus of the filtered image.

4.1. Discretization of the observable

Let P be an integer larger than $2L_k + 1$, we define

$$\left\{ \begin{array}{l} B_k^P U(\theta) = \dfrac{1}{2L_k+1} \displaystyle\sum_{\ell=-L_k}^{L_k} \frac{(\mathcal{F}_P U)_\ell \; e^{i\ell\theta}}{(-i)^\ell (J_\ell(kr_0) - iJ'_\ell(kr_0))} \\ \text{où } L_k = \max([kr_0], \left[kr_0 + (kr_0)^{\frac{1}{3}} - 2.5\right]), \end{array} \right. \tag{20}$$

with

$$(\mathcal{F}_P U)_\ell = \frac{1}{P}\sum_{p=1}^{P} U(\theta_p)e^{-i\ell\theta_p}, \qquad \text{with } \theta_p = \frac{2\pi(p-1)}{P}.$$

Operator B_k^P is a discrete approximation of the filter B_k. A straightforward calculation shows that the estimate of the norm of B_k remains true for B_k^P; indeed, we have by following the inequality of the continuous case

$$\left|B_k^P U(\theta)\right| \leq \left[\frac{1}{2L_k+1}\left(\sum_{\ell=-L_k}^{L_k}\frac{1}{J_\ell^2(kr_0)+J_\ell'^2(kr_0)}\right)^{\frac{1}{2}}\right]\left(\sum_{\ell=-L_k}^{L_k}\left|(\mathcal{F}^P U)_\ell\right|^2\right)^{\frac{1}{2}},$$

then, since $2L_k+1$ is assumed less than P, the discrete Parseval equality provides

$$\left|B_k^P U(\theta)\right| \leq \left[\frac{1}{2L_k+1}\left(\sum_{\ell=-L_k}^{L_k}\frac{1}{J_\ell^2(kr_0)+J_\ell'^2(kr_0)}\right)^{\frac{1}{2}}\right]\left(\frac{1}{P}\sum_{p=1}^{P}|U(\theta_p)|^2\right)^{\frac{1}{2}},$$

or, bounding the term between hooks by $B_\star$ (cf. appendix) and each sample $|U(\theta_p)|$ by the maximum of $|U|$

$$\left|B_k^P U(\theta)\right| \leq B_\star \|U\|_{L^\infty(0,2\pi)}.$$

To evaluate the number of samples necessary to a good approximation, we split the observable as follows

$$U(\theta) = U_P(\theta) + U_P^\perp(\theta), \quad U_P(\theta) = \sum_{\ell=-M}^{M}(\mathcal{F}U)_\ell\, e^{i\ell\theta}, \text{ with } M = \frac{P-1}{2}.$$

Remark that (as $M > L_k$) the Fourier coefficients of U_P are calculated exactly by our equidistributed quadrature rule: we have $(\mathcal{F}_P U_P)_\ell = (\mathcal{F}U_P)_\ell$, which implies that $B_k^P U_P$ coincides with $B_k U_P$. Thus,

$$\begin{aligned} B_k^P U(\theta) &= B_k^P U_P(\theta) + B_k^P U_P^\perp(\theta) = B_k U_P(\theta) + B_k^P U_P^\perp(\theta) \\ &= B_k U(\theta) + (B_k^P - B_k)U_P^\perp(\theta); \end{aligned}$$

but since $B_k U_P^\perp$ vanishes (as $M > L_k$ again), it remains

$$B_k^P U(\theta) = B_k U_P(\theta) + B_k^P U_P^\perp(\theta),$$

whence

$$|B_k^P U(\theta) - B_k U(\theta)| \leq B_\star \sup_\theta |U_P^\perp(\theta)|.$$

Assuming that P is large enough for the sup of the remaining part to be small, we have that the function $B_k^P U(\theta)$ is, when $U(\theta)$ is the trace of some perturbed plane waves, the weighted sum of a linear combination of sinc like functions $\psi_{L_k}(\theta-\theta_p)$ plus a perturbation (sum of the noise raised with the error induced by the discretization). It is then possible to proceed again as in the §2.3 and shows that the supremum is reached at a point localized in a confidence interval of size $\frac{\pi}{L_k+\frac{1}{2}}$ around the the angle of incidence.

Given ϵ small, it is therefore sufficient to choose P such that

$$\sup_\theta |U_P^\perp(\theta)| \leq \epsilon |b_1|.$$

If U is the observable associated to the plane wave $b_1 e^{-ikr\cos(\theta-\theta_1)}$, this is equivalent to

$$\sup_\theta \left| \sum_{\ell>M} (J_\ell(kr_0) - iJ'_\ell(kr_0)) i^\ell \cos \ell\theta \right| \le \epsilon, \quad M = \frac{P-1}{2}.$$

This problem has been the subject of many studies in the framework of the "*Fast Multipole Method*". For instance, using the techniques developed in [7], it can be shown that when kr_0 is larger than 10 then, taking $P > 2M^\epsilon(kr_0) + 1$ points with

$$M^\epsilon(kr_0) = \left[kr_0 + \frac{1}{2}\left(\frac{3}{2} W\left(\frac{2}{3\pi\varepsilon^2}\right)\right)^{\frac{2}{3}} (kr_0)^{\frac{1}{3}} \right] + 2, \tag{21}$$

The function $W(u)$ is the *Lambert function* defined as the unique solution of

$$W(u)e^{W(u)} = u \tag{22}$$

(this function has a sub-logarithmic behavior when u tends toward infinity). We get

$$\sup_\varphi \left| \sum_{\ell > M^\epsilon(kr_0)} (J_\ell(kr_0) - iJ'_\ell(kr_0))(-i)^\ell e^{i\ell\varphi} \right| < 2\epsilon.$$

A Numerical study shows that the constant in front of $(kr_0)^{\frac{1}{3}}$ in (21) is, respectively, 3.24, 49.37 and 156.01 for $\epsilon = 10^{-2}$, $\epsilon = 10^{-6}$ and $\epsilon = 10^{-10}$. If we compare with L_k in filter (20), we see that it is always necessary choose $M^\epsilon(kr_0) > L_k$, that is more samples than Fourier coefficients.

Remark: The same approach can be followed to study the discretization in the point source case. Ones uses in this case truncature error estimates in the Graf'series that have been also studied in the *Fast Multipole Method*. The estimates for the $M^\epsilon(kr_0)$ are of the same kind but with constants in front of the term in $(kr_0)^{\frac{1}{3}}$ which depends now on $\frac{r_0}{R}$, see [6].

4.2. Taking the maximum over a finite set of samples

The natural and practical post processing of the `NMLA` output consist in selecting the supremum of $B_k U_k$ over a finite number of discretization angles. We are interested here in the evaluation of the number of samples Q needed to capture it accurately.

First, we know that before discretization, the size of the confidence interval linked to the truncation to $2\,L_k + 1$ is $\frac{\pi}{L_k + \frac{1}{2}}$. So a uniform discretization of size Q should be chosen such that there is least one sample in every interval of this length. We need

$$Q \ge 2L_k + 1.$$

Let us proceed for a single plane wave; the discretization of the image of the `NMLA` operator is

$$B_k U_k(\theta_q^Q) = b_1 \Psi_{L_k}(\theta_q^Q - \theta_1) + \delta U(\theta_q^Q), \quad \theta_q^Q = \frac{2\pi(q-1)}{Q}.$$

We now discuss and use the function Ψ_{L_k} as in §2.3. For θ_q^Q outside the interval $|\theta_q^Q - \theta_1| \le \frac{\pi}{L_k + \frac{1}{2}}$, we have

$$|B_k U_k(\theta_q^Q)| \le \frac{1}{2}|b_1| + B_\star \|\delta U\|_{L^\infty}.$$

For θ_q^Q inside this interval, the supremum of our discretization is bounded below by the value taken at the sampled angle the closest to θ_1, denoted $\theta_{q_0}^Q$. We have

$$|B_k U_k(\theta_{q_0}^Q)| \geq |b_1| \Psi_L(\delta\theta) - B_\star \|\delta U\|_{L^\infty},$$

where $\delta\theta = \theta_{q_0}^Q - \theta_1$. We necessarily have

$$|\delta\theta| \leq \frac{\pi}{Q}.$$

and the inequality is an equality when the angle θ_1 is exactly at the middle of two samples.

When Q is large enough, $\delta\theta$ is close to 0 and so $\Psi_L(\delta\theta)$ is close to 1. Indeed, we have

$$\Psi_L(\delta\theta) \geq \frac{\sin[(L_k + \frac{1}{2})\delta\theta]}{(L_k + \frac{1}{2})\delta\theta} \geq 1 - \frac{1}{6}\left((L_k + \frac{1}{2})\delta\theta\right)^2,$$

which in terms of Q gives

$$\Psi_L(\delta\theta) \geq 1 - \frac{1}{6}\left(\frac{\pi(L_k + \frac{1}{2})}{Q}\right)^2.$$

Therefore we can choose Q large enough such that , for instance,

$$\Psi_L(\delta\theta) \geq \frac{3}{4},$$

then,

$$|B_k U_k(\theta_{q_0}^Q)| \geq \frac{3}{4}|b_1| - B_\star \|\delta U\|_{L^\infty} > \frac{1}{2}|b_1| + B_\star \|\delta U\|_{L^\infty}$$

and the conclusion follows as §2.3, when the noise level is small enough, see (7).

5. An extension: the Gaussian weights filter

In the case of multiple plane waves or point sources arriving at the observation with angles θ_n, the `NMLA` output is a sum of functions $\Psi_L(\theta - \theta_n)$. These functions decrease like $\frac{C}{|\theta-\theta_n|}$, which is not fast enough to avoid pollution of the (local) maxima identification for each branch of the data when angles are close.

A possible way to improve this situation is to convolute the result with a smooth window, we used a Gaussian function. It smooths the Ψ_L functions, make them decrease faster and preserves the maxima location. The modification is easily incorporated into the filter by a multiplication in the Fourier space

$$\begin{cases} B_k^g U(\theta) = \dfrac{1}{2L_k + 1} \displaystyle\sum_{\ell=-L_k}^{L_k} \dfrac{(\mathcal{F}U)_\ell \, \varpi_\ell^k \, e^{i\ell\theta}}{(-i)^\ell (J_\ell(kr_0) - iJ'_\ell(kr_0))} \\ \quad \text{with } L_k = \max(1, [kr_0], \left[kr_0 + (kr_0)^{\frac{1}{3}} - 2.5\right]), \end{cases} \tag{23}$$

with

$$\varpi_\ell^k = \frac{\hat{G}_\ell^k}{\nu_k}, \quad \nu_k = \frac{1}{2L_k + 1} \sum_{\ell=-L}^{L} \hat{G}_\ell^k, \tag{24}$$

where $\hat{G}_\ell^k$ are real positive and even coefficients. We decided on using the Fourier coefficients of a Gaussian function $G^k(\theta)$ (τ is a free parameter)

$$\hat{G}_\ell^k = e^{-\frac{1}{2}\left(\frac{\ell}{\kappa L_k}\right)^2}. \tag{25}$$

As

$$\left|\hat{G}_\ell^k\right| < 1, \quad \lim_{L_k \to \infty} \nu_k = \tau \int_0^{\frac{1}{\tau}} e^{-\frac{1}{2}\xi^2} d\xi,$$

we infer that there exists some number C_τ, independent of k such that

$$\sup_k \max_{\ell,\ |\ell| \le L_k} \varpi_\ell^k \le C_\tau,$$

and get the bound

$$\max_\theta |B_k^g U(\theta)| < B_\star C_\tau \max_\theta |U(\theta)|\,.$$

The new Gaussian weighted filter (23)-(24)-(25) enjoys the same stability properties as the original `NMLA` filter. We have good control over noise.

If we apply it to a plane wave packet we obtain

$$B_k^g U_k^{plane}(\theta) = \sum_{p=1}^{P} b_p \Psi_{L_k}^\tau(\theta - \theta_p),$$

where the new shape function Ψ_{L_k} is the convolution of the original one with the Gaussian

$$\Psi_{L_k} \star G^k(\theta) = \Psi_{L_k}^\tau(\theta) = \left(\sum_{\ell=-L^k}^{L_k} \hat{G}_\ell^k\right)^{-1} \sum_{\ell=-L_k}^{L_k} \hat{G}_\ell^k e^{i\ell(\theta-\theta_p)}.$$

When τ is not too small, each function associated to a particular angle decrease much faster. It allows to separate angle contributions when they are not too close. See the numerical study section or the examples in [2]. A detailed study of function $\psi_{L_k}^\tau$, as well as the possibility to identify analytically or numerically through non linear optimization several maxima in interfering sums of such functions is on-going work.

6. Numerical study

6.1. Noisy synthetic point source data

We use the exact solution in homogeneous space, the Hankel function. The observation point x_0 is at a distance $R = 1$ meter from the source point in the direction $(\cos\theta_i, \sin\theta_i)$. We arbitrarily chose $\theta_i = 157.77$ degrees.

In order to add correlated noise, we proceed as follows : We introduce a regular Cartesian grid on top of the observation circle. The grid step is $h = \frac{2\pi}{k}\frac{1}{n_\lambda^g}$ where k is the wave number. We use $n_\lambda^g = 5$ and $n_\lambda^g = 10$ for strong and weak noise.The data values are not taken exactly at the points uniformly sampled on the observation circle but at their closest grid points. We do not interpolate.

6.2. The test algorithm for the curvature correction

We assume 50% error on the available D estimate. So we take $R := R_- = 0.5$ meter. We first numerically estimate L_0 as a function of k such that (19) satisfies

$$\mathcal{E}'(kR_-, L) \simeq 0.01.$$

On the wavelength interval we consider we find

$$L_{real} \simeq 0.93(kR_-)^{0.763}.$$

Then we set the radius of the observation circle r_0 to be the unique solution of

$$L_{real} = kr_0 + (kr_0)^{\frac{1}{3}} - 2.5.$$

The filter (20) integer truncation level L_k is close to L_{real}. The observation points are uniformly sampled on the circle and then projected on the "noise" grid. We take $P = 2M + 2$ points where M is given by (21) where $\epsilon = 10^{-13}$. Then we apply the `NMLA` (4) discrete filter on this data and select the angle corresponding to the maximum modulus

$$\beta_p = B_k^P U_k \left(\frac{2\pi(p-1)}{P} \right) \text{ for } p = 1, \dots, P$$

(we take $Q = P$ to simplify).

We then perform the curvature analysis (§3.3). We compute the phase φ_ℓ defined by (17) being careful to unwrap the possible 2π rotations (we assume the phase cannot jump more than $\frac{\pi}{2}$ between two successive ℓ). There are different possible ways to perform the parabolic fit of $\ell \to \varphi_\ell$. We do as follows : for two values of L_e, $L_e = \frac{L_k}{2}$ and $L_e = \frac{L_k}{2} + 1$, we find the best least square parabolic fit of φ_ℓ between $-L_e$ and L_e. It determines three polynomial coefficients : the zeroth order term is a constant phase $\varphi_m(L_e)$, the first order term is the angle correction $\delta\theta_{est}(L_e)$ and the third order term can be used to compute the distance to the source $R_{est}(L_e)$ (see §3.3). We then take the mean value of the two L_e, denoted $\delta\theta_{est}$ and R_{est} and use them to correct the filter as in (18). We thus obtain new corrected value sequence β_p. Assuming the maximum in modulus is reached for $p = p\star$, the angle $\theta_{est} = \frac{2\pi(p^\star-1)}{P} + \delta\theta_{est}$ is the new approximation of the incidence angle while $\beta_{p^\star}$ approximated the asymptotic amplitude of the source point data

$$\beta_{p^\star} = B_{est}(k) \simeq B_{exact} = \frac{e^{ikD}}{\sqrt{-8i\pi kD}}$$

We present below numerical results comparing this algorithm using `NMLA` and its Gaussian weight version (§5) where we use $\tau = \sqrt{\frac{2}{7}}$.

6.3. *Numerical results*

6.3.1. For fixed k We fix the wavelength to 2.5 centimeters or $kR = 40\pi \simeq 251.32$.. Using the law found in §6.2 The radius of the observation circle is

$$r_0 \simeq 14.46 \text{ cm}.$$

The grid noise in relative L^2 norm with $h = \frac{\lambda}{10}$ is 22%. We apply B_k^P and its Gaussian weight version ($L_k = 37$) to this data. On Figure 2 we plot β_p the output of the filter versus the angle in degrees. The left column is the first `NMLA` pass, the right is the curvature correction (second `NMLA`) pass. The top row corresponds to the regular `NMLA` filter, the bottom row the Gaussian weight version. We notice that all filters peak near the correct angle. Amplitude and angles are not very accurate for the first pass (especially for the non Gaussian weight version) because The plane wave approximation error is too large for this r_0 (81% in relative L^2 norm). The maximum is reached at $\theta_i + 1.05$ degree.

The parabolic fit of (17) is presented in figure 1: we indeed observe a cloud of points around a parabola. The estimated curvature is $R_{est} = 1.1075$ meter (10% error).

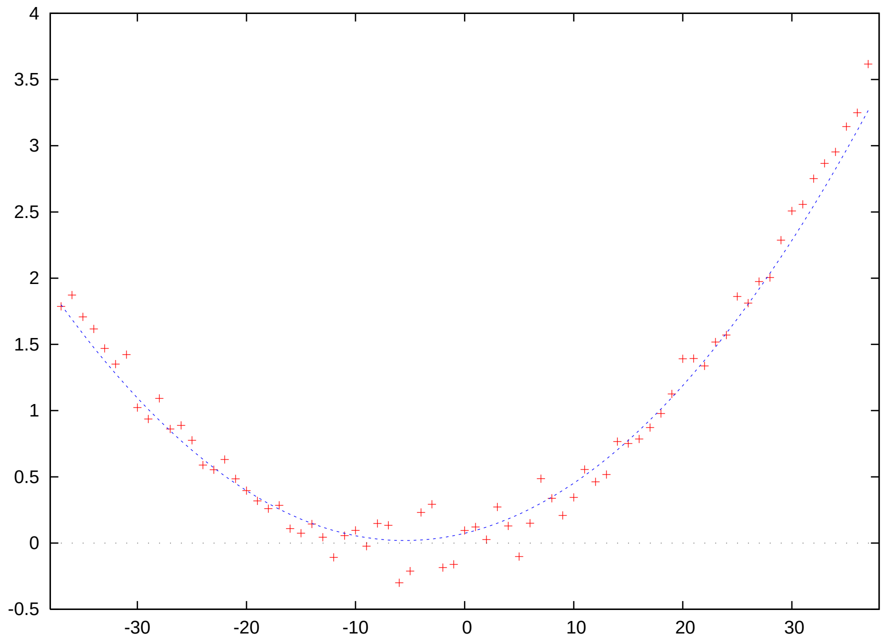

Figure 1. $\ell \mapsto \varphi_\ell$ (red crosses) and parabolic fitting (blue curve)

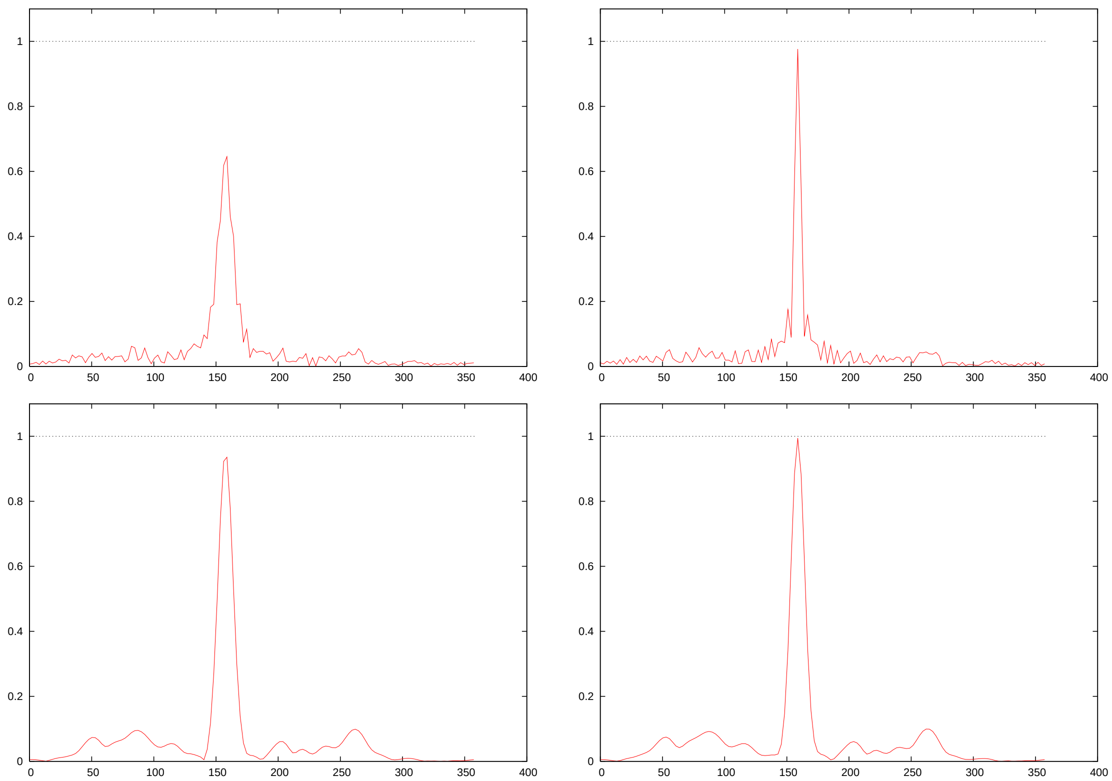

Figure 2. θ (in degree) $\mapsto \frac{|\beta(\theta)|}{|B_{exact}|}$. Left column first `NMLA` pass, right column second `NMLA` pass (curvature correction). Top row: standard filter; Bottom row : Gaussian weight filter.

The curvature correction (second pass) on the right is sharper. We get

$$\theta_{est} - \theta_i = -0.037\text{degree}, \qquad \frac{|B_{est}| - |B_{exact}|}{|B_{exact}|} \simeq -2.2\%$$

while for the Gaussian filter,

$$\theta_{est} - \theta_i = -0.037\text{degree}, \qquad \frac{|B_{est}| - |B_{exact}|}{|B_{exact}|} \simeq -0.5\%,$$

We remark that the Gaussian weight version (bottom) does a better job on the modulus of the amplitude.

One can improve this result by running the algorithm §6.2 again but with the better estimate we just found for R : $R_- = 1.10075$ meter. The result is shown in figure3. The radius r_0 is then bigger ($24.7cm$) and the new estimated curvature R_{est} is found to be 1.01 meter (1% error).

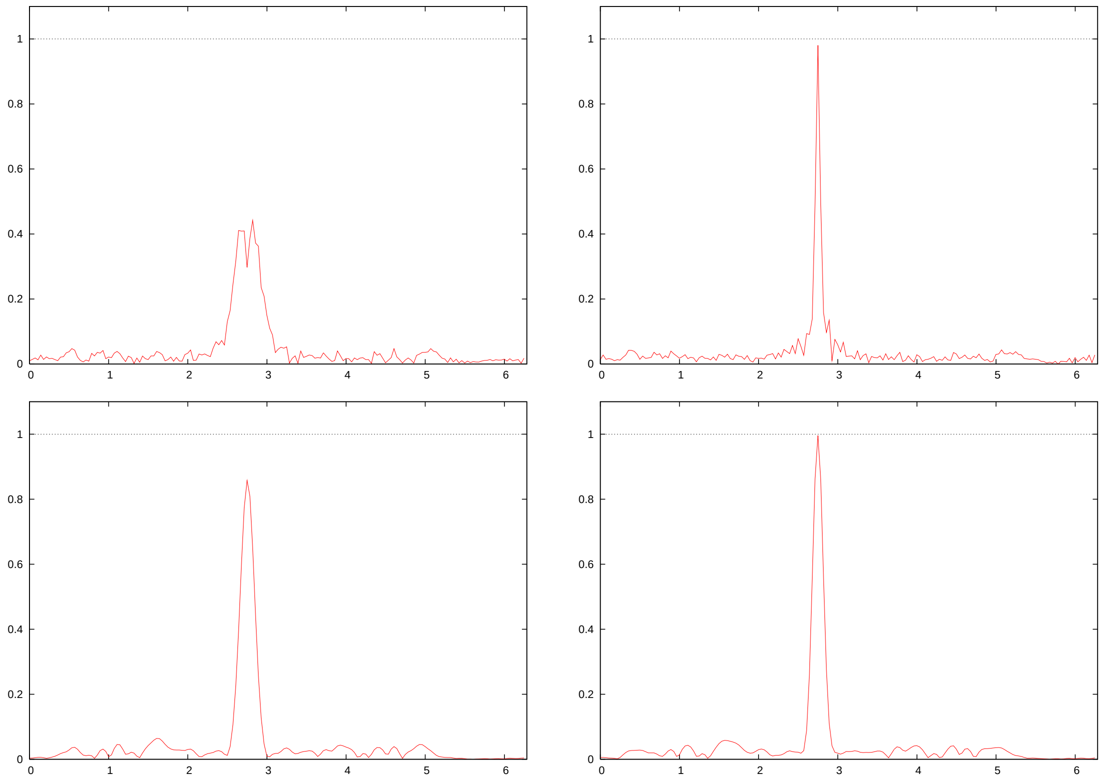

Figure 3. Same as figure 2 but with $R_- = 1.1R_{exact}$.

6.3.2. Varying k We study numerically the result of algorithm §6.2 when k takes 300 values such that the source-observation distance $R = 1$ represents between 10 and 400 wavelengths.

The "noise" grid step is one tenth of the wavelength. The relative noise level on the data varies with k between 8 and 14% (See figure 4, top).

The curvature estimate $R_{est}(k)$ varies around the exact value $R = 1$ with an error which decrease with k down to 2% from a maximum at 10% (cf. figure 4, middle).

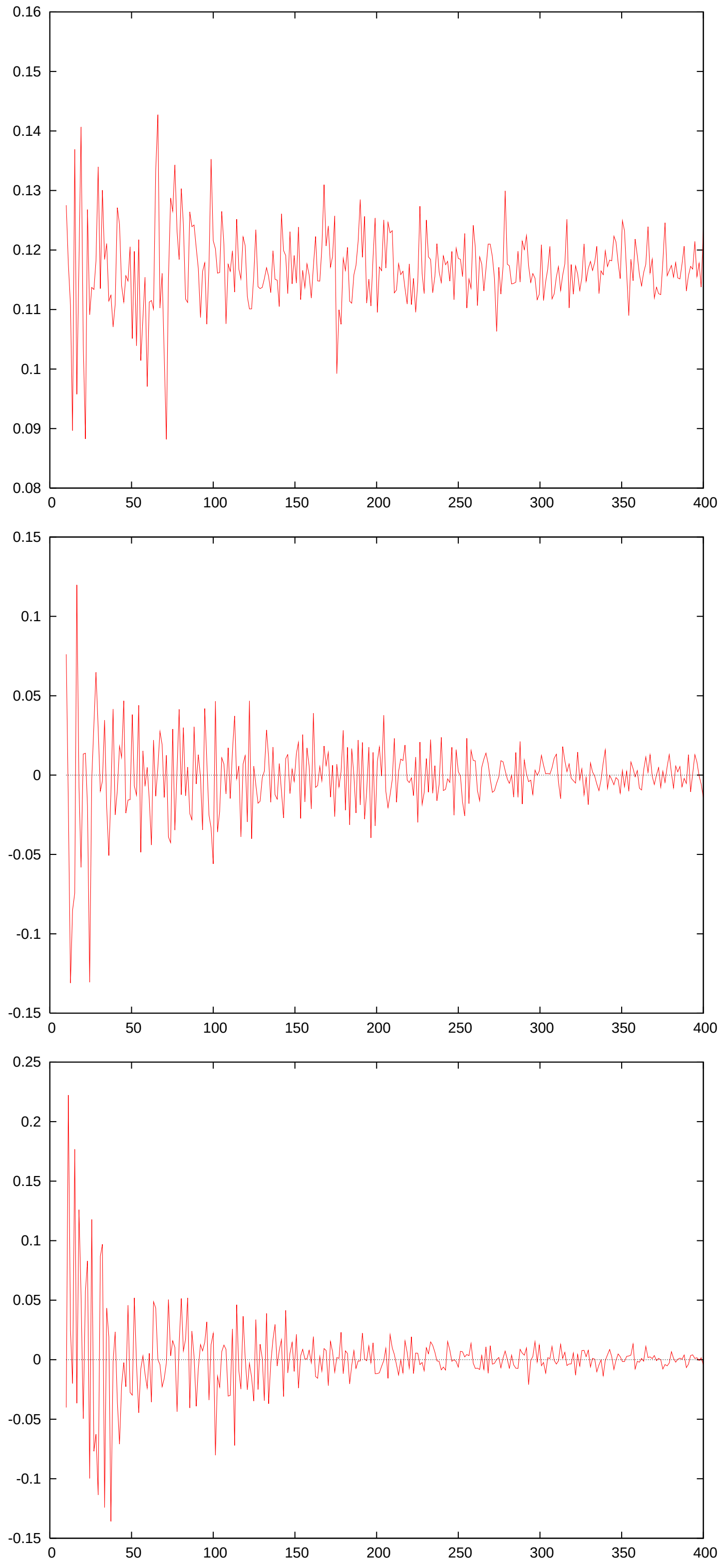

Figure 4. Top : $\frac{k}{2\pi} \mapsto \frac{|U_{noisy}(k)|_{L^2(D)} - |U_{exact}(k)|_{L^2(D)}}{|U_{exact}(k)|_{L^2(D)}}$. Middle : $\frac{k}{2\pi} \mapsto \frac{|R_{est}(k)| - R|}{R}$. Bottom : $\frac{k}{2\pi} \mapsto \theta_i - \theta_{est}(k)$.

The error on the angle (figure 4 bottom) shows a maximum of 0.2 degree but then decrease to 0.01 degree for high frequencies.

There are no noticeable differences when we use the Gaussian weight filter except on the modulus of the amplitude. Figure 5 show the relative error for this quantity which is underestimated by 0.8% for the standard `NMLA` (top) and 0.15% for the Gaussian weight filter (bottom).

References

[1] *Partial differential equations. V*, volume 34 of *Encyclopaedia of Mathematical Sciences*. Springer-Verlag, Berlin, 1999. Asymptotic methods for partial differential equations, A translation of ıt Current problems in mathematics. Fundamental directions. Vol. 34 (Russian), Akad. Nauk SSSR, Vsesoyuz. Inst. Nauchn. i Tekhn. Inform., Moscow, 1988 [MR1066954 (91e:35002)], Translation by J. S. Joel and S. A. Wolf, Translation edited by M. V. Fedoryuk.

[2] Jean-David Benamou, Francis Collino, and Simon Marmorat. Source point discovery through high frequency asymptotic time reversal. *submitted*, 2011.

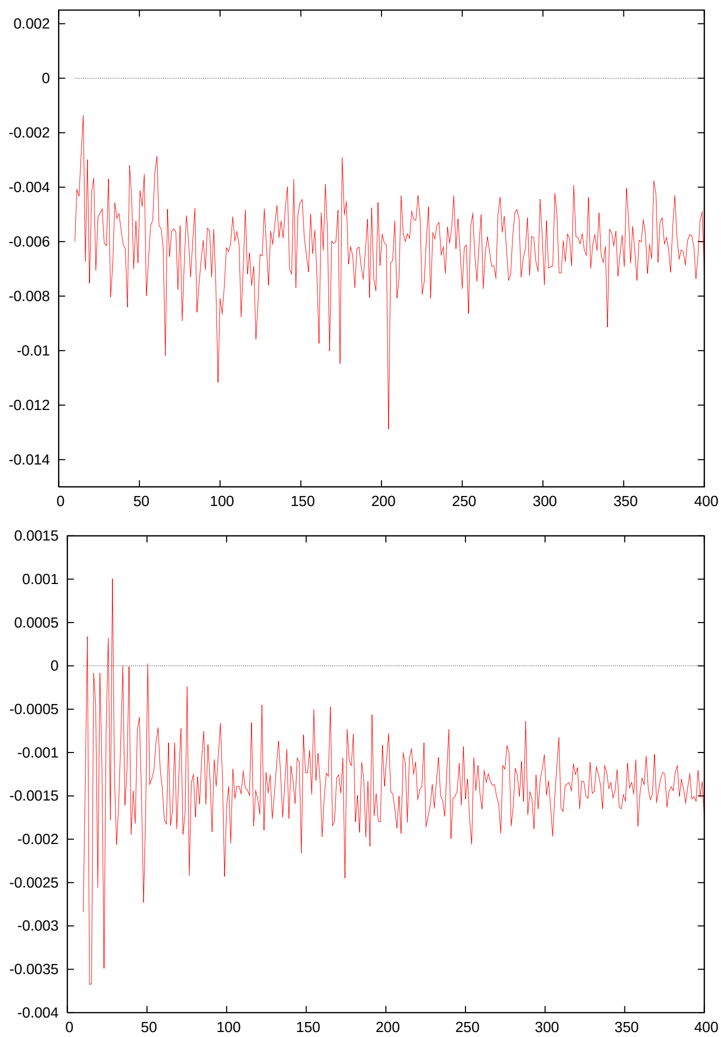

Figure 5. $\frac{k}{2\pi} \mapsto \frac{|B_{est}(k)|-|B_{exact}|}{|B_{exact}|}$. Top : standard `NMLA`. Bottom : Gaussian weight version.

[3] Jean-David Benamou, Francis Collino, and Olof Runborg. Numerical microlocal analysis of harmonic wavefields. *J. Comput. Phys.*, 199(2):717–741, 2004.
[4] Gregory Beylkin. Discrete Radon transform. *IEEE Trans. Acoust. Speech Signal Process.*, 35(2):162–172, 1987.
[5] D. Bouche, F. Molinet, and R. Mittra. *Asymptotic methods in electromagnetics.* Springer-Verlag, Berlin, 1997. Translated from the 1994 French original by Patricia and Daniel Gogny and revised by the authors.
[6] Q. Carayol and F. Collino. Error estimates in the fast multipole method for scattering problems. II. Truncation of the Gegenbauer series. *M2AN Math. Model. Numer. Anal.*, 39(1):183–221, 2005.
[7] Quentin Carayol and Francis Collino. Error estimates in the fast multipole method for scattering problems. I. Truncation of the Jacobi-Anger series. *M2AN Math. Model. Numer. Anal.*, 38(2):371–394, 2004.
[8] V. Červený. *Seismic ray theory.* Cambridge University Press, Cambridge, 2001.
[9] T.M. Cherry. Uniform asymptotic formulae for functions with transition points. *Trans. AMS*, 68:224–257, 1950.
[10] F. Collino. Conditions aux limites absorbantes d'ordre élevé pour les modèles de propagation d'onde. problème des domaines rectangulaires. Technical Report 1790, INRIA., Domaine de Voluceau, Rocquencourt, France, 1992.
[11] D. Colton and R. Kress. *Inverse Acoustic and Electromagnetic Scattering Theory*, volume 93. Springer-Verlag, 1992.
[12] Y. Landa, Nicolay M. Tanushev, and Tsai R. Discovery if point sources in the hemlhotz equation posed in unknown domains with obstacle. 2010.
[13] G. N. Watson. *A treatise on the theory of Bessel functions.* Cambridge University Press, 1966.

Appendix A. Uniform estimate in k of the filter norm

Appendix A.1. Numerical behavior of the filter norm - Optimal mode truncation law

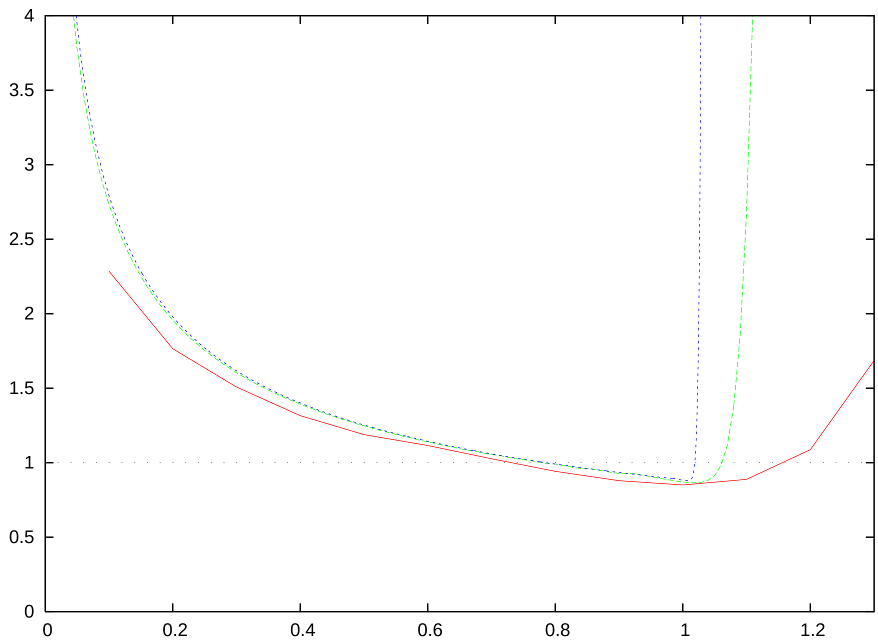

Figure A1. Sequence $L \mapsto N(L,x)$ for $x = 10$ (red), 100 (green), 1000 (blue). Horizontal axis is $\frac{L}{x}$.

We established, see (6), that the norm of the filter is bounded by the quantity

$N(L, kr_0)$ defined as

$$N^2(L,x) = \frac{1}{(2L+1)^2} \sum_{n=-L}^{L} \frac{1}{J_n^2(x) + J_n'^2(x)}.$$

A straightforward calculation gives $N^2(1,0) = 1$ and, due to the *Hansen Equality* and its variant

$$\sum_{n=-\infty}^{\infty} J_n^2(x) = 1, \qquad \sum_{n=-\infty}^{\infty} J_n'^2(x) = \frac{1}{2},$$

Cauchy Swartz provides

$$N^2(L,x) > \frac{2}{3}.$$

Now, looking at the curves $L \mapsto N(L,x)$ for a different positive values of x, the numerical computations depicted in figure A1 show that this sequence is at first decreasing on some interval $[1, L(x)]$ then increasing for L in $[L(x), +\infty[$, the increasing rate being more than exponential when L overpasses a value slightly larger than x. In Figure A2, we show the numerical behavior of functions $x \mapsto N(L,x)$ for different values of L. It appears that the minimum over all L of $N(L,x)$ remains between 0.8 and 1. It is possible to approximate numerically an optimal law $L^{opt}(x)$ for the L which minimizes $N^L(x)$. For x large enough (> 5) and less than 8000 we find

$$L^{opt}(x) \simeq x + x^{\frac{1}{3}} - 2.5.$$

So the optimal integer L for a given value of x will be

$$L^{\star}(x) = \max\left(1, [x], [x + x^{\frac{1}{3}} - 2.5]\right).$$

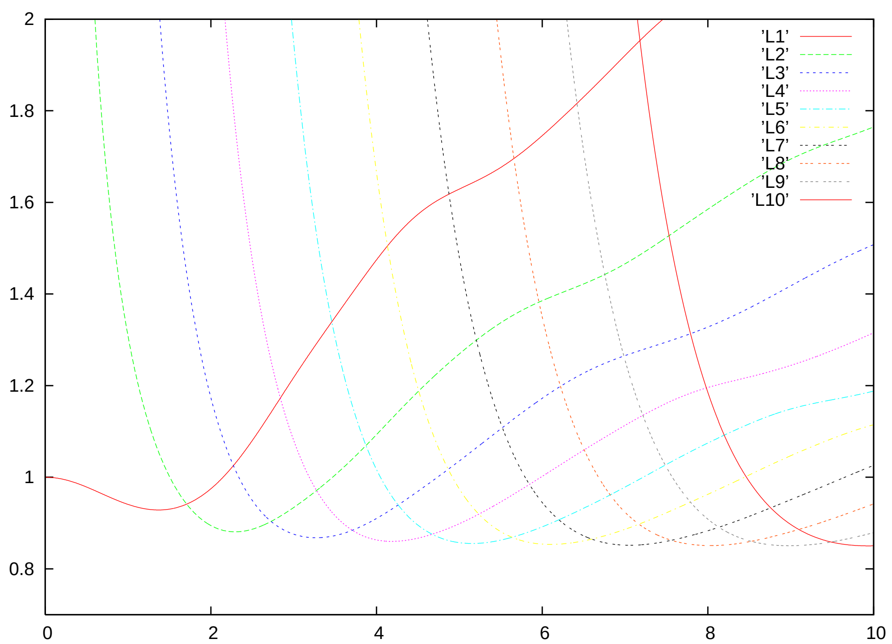

Figure A2. Functions $x \mapsto N(L,x)$ for $L = 1, \ldots 10$. For each x the lowest $N_L(x,L)$ can be read as the lowest envelop of all the curves.

Remark Long technical arguments we skipped here, give evidence that a better approximation of $L^{opt}(x)$ is

$$L^{opt}(x) \simeq \max(1, x + \left[\frac{1}{32} W^2 \left(\frac{x}{4}\left(\frac{8}{3\pi}\right)^3\right)\right]^{\frac{1}{3}} x^{\frac{1}{3}}),$$

where $u \mapsto W(u)$ is the Lambert function, see (22).

Appendix A.2. The stability result

We prove the

Theorem Appendix A.1 *Let L be a positive integer and x a positive number; let*

$$\tilde{N}^2(L,x) = \frac{1}{(L+\frac{1}{2})^2} \sum_{n=-L}^{L} \frac{1}{J_n^2(x) + J_n'^2(x)},$$

then there exists a pure constant C such that

$$\sup_{\left\{(x,L)/0 \le x \le L \le x + x^{\frac{1}{3}}\right\}} \tilde{N}^2(L,x) \le C.$$

Proof :

As a preamble, we recall that since $J_{-\ell}(x) = (-1)^\ell J_\ell(x)$, see [13, (2) page 15], we have as well

$$\tilde{N}^2(L,x) = \frac{1}{(L+\frac{1}{2})^2} \sum_{n=0}^{L} \varepsilon_\ell \frac{1}{J_n^2(x) + J_n'^2(x)},$$

where $\varepsilon_0 = 1$, and $\varepsilon_\ell = 2$ when $\ell \neq 0$. Thus, we can work with Bessel functions of non negative order.

For technical reasons, we consider separately the cases x "small" and x "large". More precisely, let x_0 be large enough to satisfy

$$x + x^{\frac{1}{3}} - x^{\frac{2}{3}} + 1 \le \sqrt{x^2 - 1}, \text{ for all } x > x_0. \tag{A.1}$$

Numerically, we find $x_0 = 4.6237...$

First, we consider the case $x < x_0$; the function $x \mapsto (x + \frac{1}{2})(J_n^2(x) + J_n'^2(x))$ is non negative and does not vanish for $x > 0$. Moreover, it tends to $\frac{2}{\pi}$ when x goes to infinity since, cf. [13, page 199]

$$J_n(x) = \sqrt{\frac{2}{\pi x}} \cos\left(x - \frac{\pi}{2}(n + \frac{1}{2})\right)\left(1 + O(x^{-1})\right),$$

$$J_n'(x) = \frac{1}{2}\left(J_{n-1}(x) - J_{n+1}(x)\right) = \sqrt{\frac{2}{\pi x}} \sin\left(x - \frac{\pi}{2}(n + \frac{1}{2})\right)\left(1 + O(x^{-1})\right).$$

We deduce that there are some constants β_n such that

$$\frac{1}{(x+\frac{1}{2})(J_n^2(x) + J_n'^2(x))} \le \beta_n,$$

and, consequently

$$\tilde{N}^2(L,x) \le \frac{x + \frac{1}{2}}{(L+\frac{1}{2})^2} \sum_{n=0}^{L} \varepsilon_n \beta_n.$$

Now, as $x < x_0$, we have if $L \leq [x + x^{\frac{1}{3}}] \leq [x_0 + x_0^{\frac{1}{3}}]$,

$$\tilde{N}^2(L,x) \leq \frac{x_0 + \frac{1}{2}}{[\frac{1}{2}]^2} \sum_{n=0}^{[x_0+x_0^{\frac{1}{3}}]+1} \varepsilon_n \beta_n = C^{ste}.$$

If the norm $\tilde{N}^2(L,x)$ diverged over $x \leq L \leq x + x^{\frac{1}{3}}$, it can only be for x large.

Consider now x large, i.e. $x > x_0$. Bounding above being easier than bounding below, we use the identity ($Y_n(x)$ is the *Neumann Function*, see [13])

$$\frac{1}{J_n^2(x) + J_n'^2(x)} = \frac{Y_n^2(x) + Y_n'^2(x)}{(J_n(x)Y_n(x) + J_n'(x)Y_n'(x))^2 + (J_n(x)Y_n'(x) - J_n'(x)Y_n(x))^2}.$$

We recognize in the second term inside the denominator the square of the Wronksian

$$J_n(x)Y_n'(x) - J_n'(x)Y_n(x) = \frac{2}{\pi x}, \tag{A.2}$$

where $Y_n(x)$ is the *Neumann Function*, [13, pp 64]; we then have

$$\frac{1}{J_n^2(x) + J_n'^2(x)} \leq \frac{\pi^2 x^2}{4} \left(Y_n^2(x) + Y_n'^2(x) \right).$$

To get rid of the derivative, we use

$$Y_n'(x) = \frac{1}{2} \left(Y_{n-1}(x) - Y_{n+1}(x) \right), \; n \neq 0, \quad Y_0'(x) = -Y_1(x)$$

and therefore

$$\frac{1}{J_n^2(x) + J_n'^2(x)} \leq \frac{\pi^2 x^2}{4} \left(Y_n^2(x) + \frac{1}{2} Y_{n-1}^2(x) + \frac{1}{2} Y_{n+1}^2(x) \right),$$

from which, we deduce (the constant π^2 is not optimal)

$$\tilde{N}^2(L,x) \leq \pi^2 \frac{x^2}{(L+\frac{1}{2})^2} \sum_{n=0}^{L+1} Y_n^2(x) \tag{A.3}$$

We are going bound above the right hand side of (A.3). We split the summation over n into four parts: $n = 0$, then $n = 1, \ldots Q$, then $n = Q+1, \ldots L-1$ and at finally $n = L, L+1$ where Q is chosen such that

$$x + x^{\frac{1}{3}} - x^{\frac{2}{3}} \leq Q < \sqrt{x^2 - 1}.$$

Such an integer does exist because the difference between the upper and lower bounds is always larger than 1 when $x > x_0$ (x_0 was precisely chosen for that). In the following, we will often use the square of the modulus of the Hankel function $J_n(x) + iY_n(x)$ since one controls rather well its behavior, thanks to the *Nicholson formulae*, [13, page 444]

$$J_n^2(x) + Y_n^2(x) = \frac{8}{\pi} \int_0^\infty K_0(2x \sinh t) \cosh(2nt) \, dt.$$

(i) For $n = 0$: as $x \mapsto J_n^2(x) + Y_n^2(x)$ is a decreasing function, [13, page 446]. So, for $x \in [x_0, ; \infty]$

$$Y_0^2(x) \leq J_0^2(x_0) + Y_0^2(x_0) = C_0. \tag{A.4}$$

(ii) For $n = 1, \dots Q$: we use [13, page 447], when $x \geq n \geq \frac{1}{2}$

$$J_n^2(x) + Y_n^2(x) \leq \frac{2}{\pi} \frac{1}{\sqrt{x^2 - n^2}},$$

and therefore

$$\sum_{n=1}^{Q} Y_n^2(x) \leq \frac{2}{\pi} \sum_{n=1}^{Q} \frac{1}{\sqrt{x^2 - n^2}},$$

but, since the sequence $n \mapsto \frac{1}{\sqrt{x^2-n^2}}$ is increasing, we have

$$\sum_{n=1}^{Q} J_n^2(x) + Y_n^2(x) \leq \frac{2}{\pi} \left(\frac{1}{\sqrt{x^2 - Q^2}} + \int_0^Q \frac{d\nu}{\sqrt{x^2 - \nu^2}} \right),$$

or

$$\sum_{n=1}^{Q} J_n^2(x) + Y_n^2(x) \leq \frac{2}{\pi} \left(\frac{1}{\sqrt{x^2 - Q^2}} + \left[\arcsin \frac{\nu}{x} \right]_{\nu=0}^{Q} \right) \leq \frac{2}{\pi} \left(\frac{1}{\sqrt{x^2 - Q^2}} + \pi \right).$$

Now, one's recall that the Q was chosen such that $Q \leq \sqrt{x^2 - 1}$ and therefore $\frac{1}{\sqrt{x^2-Q^2}} \leq 1$; we deduce

$$\sum_{n=1}^{Q} J_n^2(x) + Y_n^2(x) \leq \frac{2}{\pi}(1 + \pi) = C_1. \tag{A.5}$$

(iii) For $n = Q + 1, \dots L - 1$: function $\nu \mapsto J_\nu^2(x) + Y_\nu^2(x)$ is increasing (cf. Nicholson formulae), we thus have

$$\sum_{n=Q+1}^{L-1} Y_n^2(x) \leq \sum_{n=Q+1}^{L-1} J_n^2(x) + Y_n^2(x) \leq (L - Q) \left(J_{L-1}^2(x) + Y_{L-1}^2(x) \right).$$

But if $L \leq x + x^{\frac{1}{3}} + 1$, we have

$$\sum_{n=Q+1}^{L-1} J_n^2(x) + Y_n^2(x) \leq (L - Q) \left(J^2_{x+x^{\frac{1}{3}}}(x) + Y^2_{x+x^{\frac{1}{3}}}(x) \right) = (L - Q)\psi(x).$$

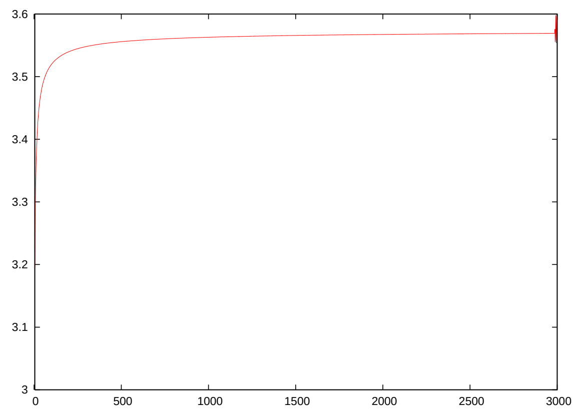

Figure A3. Graph of Function $x^{\frac{2}{3}}\psi(x)$ over $x \in [4, 3000]$

The behavior of function $\psi(x)$ for x large can be deduced from the approximations of Bessel's Functions which argument is closed to its order. From the estimates given in [9], we deduce (painfully) that when κ is given and x is large,

$$J_{x+\kappa x^{\frac{1}{3}}}(x) \simeq \left(\frac{2}{x}\right)^{\frac{1}{3}} \mathrm{Ai}(2^{\frac{1}{3}}\kappa), \quad Y_{x+\kappa x^{\frac{1}{3}}}(x) \simeq \left(\frac{2}{x}\right)^{\frac{1}{3}} \mathrm{Bi}(2^{\frac{1}{3}}\kappa),$$

Where Functions Ai and Bi are the *Airy Functions* . Thus (cf. Fig A3), there exists a constant C_2 such that

$$\sup_{x>x_0} x^{\frac{2}{3}} \left(J^2_{x+x^{\frac{1}{3}}}(x) + Y^2_{x+x^{\frac{1}{3}}}(x)\right) \leq C_2,$$

and therefore

$$\sum_{n=Q+1}^{L-1} J_n^2(x) + Y_n^2(x) \leq \frac{(L-Q)}{x^{\frac{2}{3}}} C_2 \leq C_2, \tag{A.6}$$

The last equality coming from the bound

$$L - Q \leq x + x^{\frac{1}{3}} - (x + x^{\frac{1}{3}} - x^{\frac{2}{3}}) = x^{\frac{2}{3}}.$$

(iv) For the two last terms of the series L, $L+1$: in order to use the previous estimate, we move back twice on the order of the Bessel functions . Since

$$Y_{n+1}(x) = -Y_{n-1}(x) + \frac{2n}{x} Y_n(x),$$

we have

$$\frac{1}{2} Y^2_{n+1}(x) \leq Y^2_{n-1}(x) + \frac{4n^2}{x^2} Y_n^2(x),$$

and, by successive bounding, we get

$$Y_n^2(x) + Y^2_{n+1}(x) \leq 2\left(1 + \frac{8n^2}{x^2}\left(1 + \frac{4(n-1)^2}{x^2}\right)\right) \max\left(Y^2_{n-2}(x), Y^2_{n-1}(x)\right).$$

and therefore

$$Y_n^2(x) + Y^2_{n+1}(x) \leq 2\left(1 + \frac{8n^2}{x^2}\left(1 + \frac{4n^2}{x^2}\right)\right) \left(Y^2_{n-1}(x) + J^2_{n-1}(x)\right)$$

and that, always thanks to the increasing property of the sequence $n \mapsto J_n^2(x) + Y_n^2(x)$. We are brought to the previous bound. Thus, we have, when $L < x + x^{\frac{1}{3}}$

$$\sum_{n=L}^{L+1} Y_n^2(x) \leq 2\left(1 + \frac{8L^2}{x^2}\left(1 + \frac{4L^2}{x^2}\right)\right)(J^2_{x+x^{\frac{1}{3}}}(x) + Y^2_{x+x^{\frac{1}{3}}}(x)),$$

or also, when $x_0 \leq x \leq L \leq x + x^{\frac{1}{3}}$,

$$\sum_{n=L}^{L+1} Y_n^2(x) \leq 2\left(1 + \frac{8(x+x^{\frac{1}{3}})^2}{x^2}\left(1 + \frac{4(x+x^{\frac{1}{3}})^2}{x^2}\right)\right)\frac{C_2}{x^{\frac{2}{3}}} \leq C_3. \tag{A.7}$$

We gather all our results, when $x + x^{\frac{1}{3}} > L > x > x_0$, there exists four constants such that

$$\tilde{N}^2(L,x) \leq \pi^2 \frac{x^2}{(L+\frac{1}{2})^2}(C_0 + C_1 + C_2 + C_3) \leq \pi^2 (C_0 + C_1 + C_2 + C_3),$$

and since $\tilde{N}^2(L,x)$ is uniformly bounded over $x \leq x_0$ and $L \leq [x_0 + x_0^{\frac{1}{3}}]$,

Q.E.D. □

Source point discovery through High Frequency Asymptotic Time Reversal

Jean-David BENAMOU - Francis COLLINO - Simon MARMORAT

January 18, 2011

Abstract

Given local frequency domain wave data, the Numerical MicroLocal Analysis (NMLA) method [7] in its recent improved version [6] gives a pointwise estimate of the number of rays, their slowness vectors and corresponding wavefront curvatures. With time domain wave data and assuming the source wavelet is given, the method also estimates the traveltime. The paper provides a pedestrian presentation of the NMLA algorithm and a numerical application which can be interpreted as a High Frequency asymptotic version of the classical Time Reversal method [9].

keyword : Linear Waves, Geometrical Optics, Time Reversal

1 Introduction

Source point or scatterer location identification is a classical inverse problem in computational wave propagation. It is of great practical interest in, for example, non destructive testing of alloys defect, kidney stones location discovery [15], underwater communications [30]. It is a basic step in inverse synthetic aperture radar [10]. See also [25] for the same problem of source discovery.

The popular time reversal (TR) method (see [9] for a mathematical study and references) solves this inverse problem. It is rapidly summarized in the following steps :

(i) record a wave signal on some array of "transducers" for "some" time

(ii) time reverse this signal and re-emit it in the medium.

Then, physics observes and maths proves that the time reversed signal will exhibit refocusing properties towards the scatterers or the source points depending on the set up of the experiment.

We propose a new interpretation of time reversal using the High Frequency (HF) asymptotic model of wave propagation, also known as Geometric Optics (GO). The HF model only makes sense with smooth deterministic media when the characteristic wavelength of the signal is smaller than the variation scale of the acoustic speed. We will therefore NOT be concerned with the widely studied "super-resolution" effect of the focusing observed in random media [9].

The goal of the paper is twofold :

- Provide a non technical description of the Numerical MicroLocal Analysis algorithm (NMLA) [7] and its recent improved second order version [6]. We apply it to analyze the underlying GO ray directions of the signal recorded in step (i). The NMLA algorithm works in the frequency domain. We therefore use classic pre and post processing techniques to extend it to time domain and also to treat a signal recorded on linear arrays of transducers. We also show that the use of time domain data simplify multiple rays discrimination and that frequency redundant information provides a traveltime estimate from the source.
- Demonstrate numerically that the output ray direction and traveltime are accurate enough, at least with synthetic noisy data, to shoot the ray back to its unknown source location. The notion of "shooting back" implies that the traveltime, the actual propagation time, is reversed in the same way as in step (ii) above.

In order to make the paper self contained, it is organized as follows :

Section 2 recalls the HF model derivation and formulates the HF asymptotic time reversal source discovery inverse problem.

Section 3 reviews the refined NMLA algorithm [6] and its extension to time domain data recorded on a linear array of "transducers".

Section 4 presents numerical source discovery from synthetic data.

2 Forward and inverse Problem

2.1 High frequency acoustic wave equation

We start from the classical acoustic wave equation in the time domain. The wave field $u(x,t)$ is generated by a finite time wavelet emitting from a source point :

$$(P)\left\{\begin{array}{l}\dfrac{1}{c^2(x)}\partial^2_{tt}u(x,t)-\Delta u(x,t)=\delta(x-x_s)\,W_{\omega_s}(t),\ \forall(x,t)\in\mathbb{R}^2\times[0,T)\\ u(x,t=0)=\partial_t u(x,t=0)=0,\ \forall x\in\mathbb{R}^2,\end{array}\right. \tag{1}$$

where

- $[0,T)$ is the simulation time (one may consider $T=+\infty$)
- $x\mapsto c(x)$ is the acoustic speed law function on $\mathbb{R}^2$. As we deal with HF GO models, we will consider smooth speeds.
- x_s is the source point location
- $t\mapsto W_{\omega_s}(t)$ is the source time wavelet.

In all the sequel the radian frequency ω will be the dual variable of time in the Fourier transform denoted $\hat{}$:

$$\hat{u}(x;\omega)=\int_0^\infty u(x,t)\,e^{i\omega t}\,dt. \tag{2}$$

The frequency content of the solution depends on the source wavelet's. HF wave fields have strong HF content. It can be tuned using the "characteristic pulsation (or frequency)" ω_s which parametrizes $W_{\omega_s}(t)$. More precisely, we set

$$W_{\omega_s}(t)=W(\omega_s\,t),$$

where $W(t)$ is a shape function with support in $[0,1]$. Assuming further that W is absolutely integrable and has zero mean, the following properties can be checked :

$$\text{Support }(W_{\omega_s})=[0,\frac{1}{\omega_s}]. \tag{3}$$

$$\hat{W}_{\omega_s}(\omega)=\frac{1}{\omega_s}\hat{W}\left(\frac{\omega}{\omega_s}\right). \tag{4}$$

For $\epsilon > 0$, there exists two positive constants γ_ϵ^+ and γ_ϵ^- such that

$$\int_{\omega \notin I} |\hat{W}_{\omega_s}(\omega)|^2 d\omega \leq \epsilon \int |\hat{W}_{\omega_s}(\omega)|^2 d\omega, \quad I = [\gamma_\epsilon^- \omega_s, \gamma_\epsilon^+ \omega_s] \tag{5}$$

So when ω_s tends to infinity, (3) shows that the source impulse lapse shrinks and (4-5) that the frequency content becomes large and is shifted to infinity.

2.2 Frequency domain and ansatz

The HF model uses a formal asymptotic representation of the solution, where the unknowns are independent of the radian "frequency" ω. It is easier to derive and interpret it in the frequency domain :

Assume $T = +\infty$ and Fourier transform (see (2)) equation (1) :

$$-\frac{\omega^2}{c^2(x)} \hat{u}(x;\omega) - \Delta \hat{u}(x;\omega) = \delta(x - x_s)\, \hat{W}_{\omega_s}(\omega). \tag{6}$$

We consider that $c(x) = v$ is constant outside a compact in Ω, and add the Sommerfeld radiation boundary condition at infinity

$$\lim_{|x| \to \infty} \partial_{|x|} \hat{u}(x;\omega) - \frac{i\omega}{v} \hat{u}(x;\omega) = 0, \tag{7}$$

to ensure uniqueness [19].

In the homogeneous case ($c(x) = v$ constant everywhere), the analytic solution of (6-7) is given by

$$\hat{u}(x;\omega) = \frac{i}{4} H_0^{(1)} \left(\omega \frac{|x - x_s|}{v} \right) \hat{W}_{\omega_s}(\omega), \tag{8}$$

where $H_0^{(1)}(u)$ is the Hankel function of first type and order 0. Using the following asymptotic estimate (cf. [31])

$$H_0^{(1)}(x) \underset{x \to \infty}{\sim} \sqrt{\frac{2}{\pi x}} e^{i(x - \frac{\pi}{4})},$$

in (8), we obtain the asymptotic approximation of the solution

$$\hat{u}(x;\omega) \simeq A(x;x_s) e^{i\omega\phi(x,x_s)} \frac{\hat{W}_{\omega_s}(\omega)}{\sqrt{-i\omega}}, \tag{9}$$

where the large parameter is the number of wavelengths between the source and the observation point (the product $\omega\frac{|x-x_s|}{v}$) and A and ϕ are the GO solution (see next section) :

$$A(x,y) = \sqrt{\frac{v}{8\pi|x-y|}}, \quad \phi(x,y) = \frac{|x-y|}{v}. \tag{10}$$

The "ansatz" idea, apparently going back to a 1911 paper of Debye on "the article of Sommerfeld" (see [1]), consists in generalizing the a priori form (9) to the general heterogeneous case and search for a *formal asymptotic solution* of the Helmholtz equation in the form

$$\hat{u}^{ray}(x;\omega) \simeq e^{i\omega\varphi(x)} \sum_{j=0}^{\infty} \frac{A_j(x)}{(i\,\omega)^j}, \tag{11}$$

(we assume the source wavelet and the half primitive (symbol $\sqrt{-i\omega}$) have been removed, see section 3.1).

In general, only the first A_0 term of the amplitude series is used. Oscillations are formally enforced in the phase and travel at traveltime φ. The radian frequency ω is the large parameter.

2.3 Geometric optics - Ray tracing

Assuming a solution taking the ansatz form (11) locally away from the source. One can plug it into

$$\Delta\hat{u}(x;\omega) + \frac{\omega^2}{c^2(x)}\hat{u}(x;\omega) = 0, \tag{12}$$

and expand in inverse power of ω. Canceling the coefficients of the first and second order term of the series gives respectively the Eikonal equation and amplitude equations

$$\begin{cases} |\nabla\varphi(x)| = \dfrac{1}{c(x)} \\ 2\nabla\varphi(x)\cdot\nabla A_0(x) + A_0(x)\Delta\varphi(x) = 0. \end{cases} \tag{13}$$

These equations are local but global solutions are constructed using a Lagrangian method called Ray Tracing.

The traveltime φ is computed along the integral curves of the gradient called rays and denoted $s \to y(s, y_0)$. Each ray may be parameterized by its initial position y_0 and assuming the traveltime and its gradient are known at this location one solves the following system of ODEs :

$$\begin{cases} \frac{d}{ds} y(s, y_0) = \nabla\varphi(y(s, y_0)) := p(s, y_0),\ y(0, y_0) = y_0, \\ \\ \frac{d}{ds} p(s, y_0) = \frac{1}{2}\nabla n^2(y(s, y_0)),\ p(0, y_0) = \nabla\varphi(y_0) \text{ given}, \\ \\ \frac{d}{ds}\varphi(y(s, y_0)) = n^2(y(s, y_0)),\ \varphi(y_0) \text{ given}, \end{cases} \tag{14}$$

where

- $y(s, y_0)$ is the ray shot from y_0 and s is a parameterization of the curve.
- $p = \nabla\phi(y)$ is called the "slowness" vector and gives the ray direction.
- $n = \frac{1}{c}$ is called the slowness of the medium.

When the velocity is homogeneous ($c(x) = v$) around a source point, the analytic asymptotic form (10) may be used to define the initial conditions : For τ small enough the level curve $W_C = \{y_0,\ \text{s.t. } \phi(y_0) = \frac{|y_0 - x_s|}{v} = \tau\}$ is a circle around the source point and $p(0, y_0) = \nabla\varphi(y_0) = \frac{(y_0 - x_s)}{v\,|y_0 - x_s|}$. Letting τ go to 0 we consider that the HF asymptotic form of a source point corresponds to rays leaving the source point x_s isotropically with the same amplitude. We then switch the parameterization of the rays to the initial take off angle $y_0 \to \theta_0$. The global HF solution is formed of all rays; this is the solution, for all $\theta_0 \in [0, 2\pi[$, of

$$\begin{cases} \frac{d}{ds} y(s, \theta_0) = \nabla\varphi(y(s, \theta_0)) := p(s, \theta_0),\ y(0, \theta_0) = x_s \\ \\ \frac{d}{ds} p(s, \theta_0) = \frac{1}{2}\nabla n^2(y(s, \theta_0)),\ p(0, \theta_0) = \dfrac{\tilde{s}_0}{v} \\ \\ \frac{d}{ds}\varphi(y(s, \theta_0)) = n^2(y(s, \theta_0)),\ \varphi(x_s) = 0, \end{cases} \tag{15}$$

where $\tilde{s}_0 = (\cos\theta_0, \sin\theta_0)$.

Ray Tracing (14-15) can be extended to compute solutions of the amplitude equation (see [5] for instance).

In smooth heterogeneous media, the Lagrangian traveltime function remains smooth but it is quite common for rays to cross. Then, solutions to the Eulerian equation (13) become multivalued. In the simplest case, the HF ansatz remains a superposition/sum of elementary (11) ansatz. See [21] [5] for more details and references on multivalued solutions. In this paper and also for the NMLA algorithm we will always assume that the Helmholtz solution has a general HF representation of the form

$$\hat{u}(x;\omega) \simeq \sum_{n=1}^{N} A_{0,n}(x) e^{i\omega\varphi_n(x)}, \tag{16}$$

where N is the number of rays going through x and n the subscript labeling the different branches of the solution. We kept only the zeroth order term of the amplitude series of (11).

2.4 Source point discovery with HF time reversal

We now propose an HF local interpretation of the time reversal algorithm $(i)-(ii)$:

$(i)_{HF}$ Record an acoustic signal around some observation point x_0 and for "some" time; this will be our data. Then, identify at least one significant ray going through x_0, its traveltime and slowness vector. Let us denote them $\varphi^{data}(x_0)$ and $p_0^{data} = \nabla\varphi^{data}(x_0)$.

$(ii)_{HF}$ Time reverse this signal and re-emit it in the medium using the HF model. This is accomplished by changing ds in $-ds$ (15) and use the initial conditions obtained in $(i)_{HF}$ for this particular ray :

$$\begin{cases} \frac{d}{-ds} y(s) = \nabla\varphi(y(s)) := p(s),\ y(0) = x_0 \\ \frac{d}{-ds} p(s) = \frac{1}{2}\nabla n^2(y(s)),\ p(0) = p_0^{data} \\ \frac{d}{-ds}\varphi(y(s)) = n^2(y(s,\theta_0)),\ \varphi(x_s) = \varphi^{data}(x_0). \end{cases} \tag{17}$$

The traveltime $\varphi(y(s))$ will then decrease and we stop integrating (17) when it gets to 0. If step $(i)_{HF}$ yields a reliable HF component estimate, we have time reverted the ray and $y(s)$ has reached the source x_0.

There are no theoretical or numerical difficulties with step $(ii)_{HF}$. The next section presents the NMLA algorithm as a way to invert the ansatz (16) in order to perform step $(i)_{HF}$

3 Numerical MicroLocal Analysis [7] [6]

We assume frequency domain data $\hat{u}(x, \omega)$ is available locally on a circle around an observation point x_0. Appendix A explains in details how this format can be generated from time domain data recorded on a linear array[1].

NMLA does not directly invert (16) but a linear equation obtained through the successive steps described in the following subsections.

3.1 Source deconvolution

When the wavelet W_{ω_s} is known, one can perform the following source deconvolution on the data

$$\hat{u}(x; \omega) \leftarrow \frac{\sqrt{-i\omega}}{\hat{W}_{\omega_s}(\omega)} \hat{u}(x; \omega). \tag{18}$$

We will keep the same notation for the data. See appendix B on getting rid of this step when the source wavelet is unknown.

3.2 Plane wave approximation

We linearize the traveltime around x_0. In the GO regime, we expect the phase and amplitude to be smooth real with variations on a scale larger than ω. Using a Taylor expansion on the traveltime and within a few wavelength of x_0 we have

$$\varphi(x) \simeq \varphi(x_0) + (x - x_0) \cdot \nabla\varphi(x_0) + \frac{1}{2}(x - x_0)^T H\varphi(x_0)\,(x - x_0) + ... \tag{19}$$

The usual first order "plane wave" approximation gives, for $N = 1$ in (16),

$$\hat{u}(x; \omega) \simeq B(x_0) e^{i\omega(x-x_0)\cdot\nabla\varphi(x_0)}, \tag{20}$$

[1]A common acquisition geometry, seismogram in geophysics for instance.

where

$$B(x_0) = A_0(x_0)e^{i\omega\varphi(x_0)}.$$

In the more general case where N rays cross at x_0 we assume $\hat{u}$ can be identified as the N-rays ansatz

$$\hat{u}(x,\omega) \simeq \sum_{n=1}^{N} B_n(x_0)e^{i\omega(x-x_0)\cdot\nabla\varphi_n(x_0)}. \tag{21}$$

3.3 Relaxation

Equation (21) is non-linear, remember the unknowns are the $(B_n, \nabla\varphi_n)$ plus N the number of rays. As the norm of the gradient of the traveltimes is given by the Eikonal equation,

$$\|\nabla\varphi_n(x_0)\| = \frac{1}{c(x_0)} \quad \text{for all } n.$$

We instead consider the linear problem of finding the amplitude distribution $\{B_m,\ m = 1..M\}$ over a discretization of the set of 2-D unit vectors, $\{\tilde{d}_m = m = 1..M\}$ with

$$\tilde{d}_m = (\cos\theta_m, \sin\theta_m) \quad \theta_m = m\frac{2\,\pi}{M},\ m = 1..M \tag{22}$$

The $\tilde{.}$ notation will always refer to unit vectors. The relaxed version of (21) is

$$\hat{u}(x,\omega) \simeq \sum_{m=1}^{M} B_m(x_0)e^{i\frac{\omega}{c(x_0)}(x-x_0)\cdot\tilde{d}_m}. \tag{23}$$

The size of the discretization M is discussed later.

3.4 The observable and the Linear system

In our first paper [7] the data $\hat{u}$ was sampled on a scaled circle around x_0 using the same discretization (22).

$$U_{\alpha,m} = \hat{u}(x_0 + r\tilde{d}_m;\omega) \quad r = \frac{\alpha c(x_0)}{\omega} \quad |\tilde{s}| = 1.. \tag{24}$$

This formulation had stability issues and a L^2 regularization was used in [7]. A L^1 regularization is proposed in [25]. The new version proposed in

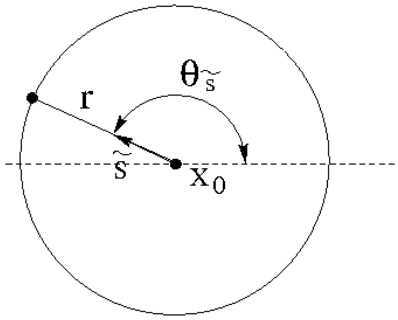

Figure 1: Geometry of the observable support, a sample point in the direction $\tilde{s}$

[6] still uses the circle geometry but the data is sampled from the impedant quantity $\frac{c(x_0)}{i\omega}\frac{\partial \hat{u}}{\partial r} + \hat{u}$. The resulting NMLA filter is stable independently of its parameters. The new observable is

$$U_m = \frac{c(x_0)}{i\omega}\frac{\partial \hat{u}}{\partial r}(x_0 + r\tilde{d}_m;\omega) + \hat{u}(x_0 + r\tilde{d}_m;\omega), \quad r = \frac{\alpha c(x_0)}{\omega}. \tag{25}$$

Modifying (23) according to this new observable and setting the vectors

$$U_\alpha = \{U_m\} \quad B_\alpha = \{B_m\} \quad m = 1,\ldots,M.$$

and the matrix

$$K_\alpha = \{(\,\tilde{s}\cdot\tilde{d}_m + 1)\,e^{i\alpha\tilde{d}_m\cdot\tilde{d}_l}\} \quad l,m = 1,\ldots,M. \tag{26}$$

The linear system to be inverted is

$$U_\alpha = K_\alpha\,B_\alpha. \tag{27}$$

3.5 K_α pseudo-inverse and stability result

The spectrum of the linear operator K_α and its continuous version have been carefully studied in [18]. In particular it can be diagonalized on the Fourier basis $\{e_l(\tilde{s}) = \frac{1}{\sqrt{2\pi}}e^{il\theta_{\tilde{s}}}\}_{l\in\mathbb{Z}}$ and its eigenvalues depend on Bessel functions

$$K_\alpha e_l = D_l(\alpha)\,e_l, \quad D_\ell(\alpha) = 2\pi i^\ell(J_\ell(\alpha) - i\ J'_\ell(\alpha));$$

$J_\ell(\alpha)$ is the Bessel function of order ℓ and argument α, it decreases more than exponentially for ℓ above a threshold which depends on α see figure 2. K_α is not invertible in any Sobolev norm but a stable and normalized pseudo-inverse can be computed as follows

$$\{B_m\} := \frac{1}{2\,L(\alpha)+1}\mathcal{F}^{-1}(\{\hat{\beta}_\ell\}), \quad \hat{\beta}_\ell = H_\ell \mathcal{F}(\{U_m\})_\ell \tag{28}$$

where :

- $\mathcal{F}$ is the M discrete Fourier transform on our discrete set of directions (22) .
- $H_\ell = D_\ell^{-1}$ if $|\ell| < L(\alpha)$ and 0 else.
- $L(\alpha)$ corresponds to a truncation threshold. It is shown in [6] that if

  $$L(\alpha) = \min\{\alpha, \alpha + \alpha^{1/3} - 2.5\} \tag{29}$$

  then the norm of the normalized inverse operator defined by (28) is bounded by 1, independently of α:

  $$\sup_m |B_m| \leq \sup_m |U_m|$$

- The sampling M must be larger than $L(\alpha)$.
- The new impedant observable (25) prevents the eigenvalues to accidentally vanish for $\ell < L(\alpha)$ (note that $J_\ell(x)$ and $J'_\ell(x)$ have no common zeros, [31]).

3.6 Exact solutions for plane wave (linear) data

When the data is a pure plane wave, i.e. linearization is exact, an analytical form of the output of NMLA is available. We denote $\tilde{d}$ the direction of the plane wave ($\theta_{\tilde{d}}$ the corresponding angle) and A the amplitude. The asymptotic HF content consists in one ray going through the observation point x_0 with the same direction. The observable data (24) is given by

$$U_m^{plwa} = B\, e^{i\alpha \tilde{d}\cdot\tilde{d}_m}, \quad m = 1, \ldots, M.$$

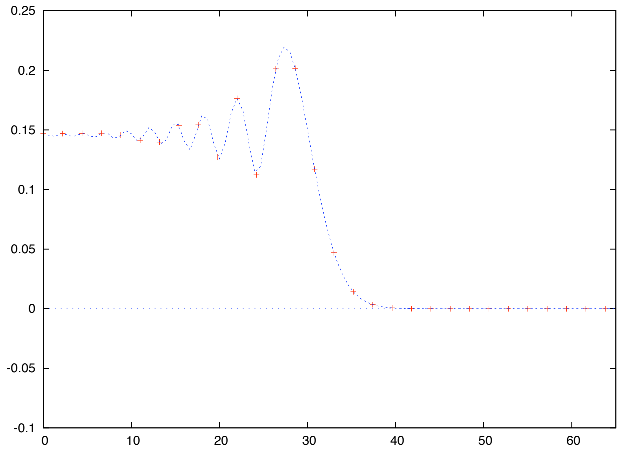

Figure 2: The stars show $|J_\ell(\alpha) - i\ J'_\ell(\alpha)|$ for integer values of ℓ and $\alpha = 30$.

The outputs of the NMLA procedure (28) is

$$\begin{cases} \hat{\beta}_\ell^{plwa} := H_\ell \mathcal{F}(\{U_\alpha^{plwa})_\ell = B\, e^{i\,\ell\,\theta_{\tilde{d}}} \\ \\ B_m^{plwa} = B\, S_\alpha(\theta_d - \theta_m)\ \ m = 1..M, \quad S_\alpha(\theta) = \frac{\sin((L(\alpha)+\frac{1}{2})\theta)}{(2L(\alpha)+1)\sin(\frac{\theta}{2})} \end{cases} \tag{30}$$

- We see that the inverse (28) is normalized such that the B_m of maximum modulus matches the amplitude of the plane wave.
- The larger the $L(\alpha)$ the more peaked the Sinc like function S_α will be.
- We note that for perfect plane wave data, a perfect ray direction approximation can be achieved by increasing M the number of sampled directions.
- As we will see in the next section this is not the case when the asymptotic wavefront has curvature or just adding noise the maximum of the peaked function is moved and a confidence interval can be estimated thanks to the stability result [6].

3.7 Second order curvature correction

As can be seen in Figure 8, $L(\alpha)$ and thus α (see (29)) bounds the number of Fourier modes and limits the accuracy as we hope to reconstruct Dirac masses in the correct ray direction. The last plot also shows that we are limited in increasing α because of both the plane wave approximation and the error linked to the second order terms in the Taylor expansion (19). We did not manage to include this term in the NMLA filter nor to use the transport equation (13). That seems to remain an open problem.

Instead, we first assume there is only one ray ($N = 1$). This is not a very restrictive assumption as both time and direction windows can be used to select a particular ray, see Appendix C. We then make the simplest non linear approximation on the HF asymptotic solution : we look for locally constant curvature as if the wavefield solution were the fundamental solution $G(x, x_s) = \frac{i}{4} H_0^{(1)}(\omega \frac{|x-x_s|}{v})$ (check (8)). The virtual source point x_s is such that $x_0 - x_s = d\tilde{d}$ where $\frac{1}{d}$ and $\tilde{d}$ are the sought for curvature of the front and direction of the ray, see figure (3).

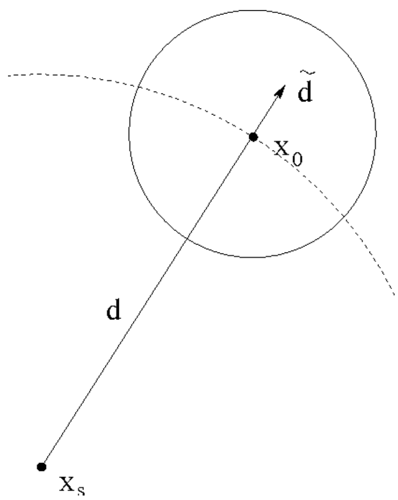

Figure 3: A constant $\frac{1}{d}$ curvature wavefront going through the observable geometry with ray direction $\tilde{d}$ at the observation point.

Then, instead of the plane wave approximation, the NMLA data is first approximated locally by a constant curvature wavefield $G(x, x_s)$. Its argument $x - x_s$ is decomposed into the sum of the main propagation direction

$(x - x_0 = d\tilde{d})$ plus $x_0 - x_s$ a vector turning around x_0 : $x_0 - x_s = r\tilde{s}$. Figure 4 present this decomposition.

$$U_\alpha(\tilde{s}) \simeq \sqrt{\frac{8\pi\, d}{c(x_0)}} A_0(x_0)\, e^{i\omega(\varphi(x_0)-d)}\, \frac{i}{4} H_0^{(1)} \left(\frac{\omega}{c(x_0)} |d\tilde{d} + r\tilde{s}| \right). \qquad (31)$$

The high frequency amplitude and phase above have been corrected as the global wavefield is not necessarily globally a point source solution in an homogeneous medium. We use the known HF asymptotics of the Hankel function, see (10).

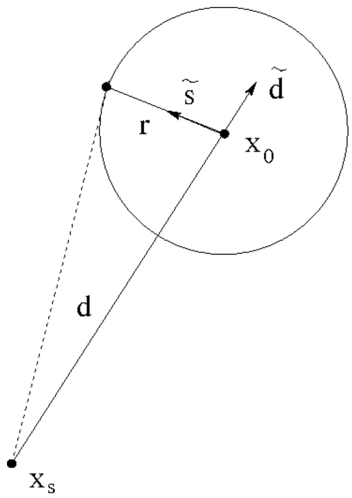

Figure 4: Observable geometry data in the direction $\tilde{s}$ on the circle is written as $d\tilde{d} + r\tilde{s}$

Inspired by asymptotic expansions from the Fast Multipole Method applied to electromagnetics [12] [13], one can then consider r as a perturbation in the argument of the Hankel function and expand the argument. Using technical asymptotic expansions, we show in [6] that a second order accurate approximation of the $\hat{\beta}$ Fourier modes of the NMLA filter (28) is

$$\hat{\beta}_\ell \simeq A e^{i\omega\varphi(x_0)} e^{i(\ell\theta_{\tilde{d}} + \frac{(\ell^2 - \frac{1}{4})}{2\gamma})}, \qquad (32)$$

where $\gamma = \frac{\omega\, d}{c(x_0)}$ is a new large parameter and $\theta_{\tilde{d}}$ is the angle associated to $\tilde{d}$. This is to be compared to the exact solution for one plane wave linear data

(30). We see that we get a γ (curvature dependent) second order correction. From there we simply remark that

$$\frac{1}{i}\log(\frac{\hat{\beta}_\ell}{\hat{\beta}_0}) \simeq \ell\theta_{\tilde{d}} + \frac{(\ell^2 - \frac{1}{4})}{2\gamma}) \tag{33}$$

is a parabolic function of the mode number ℓ and the coefficients $\theta_{\tilde{d}}$ and $\frac{1}{2\gamma}$ can be fitted by a least square approximation, see figure 5.

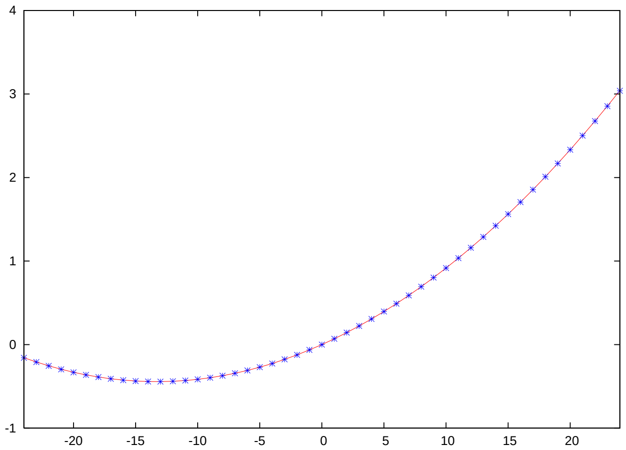

Figure 5: Blues stars are the (33) values and the red curve the fitted parabola.

We summarize the 2nd order correction of the NMLA algorithm (see figure 9 for a numerical illustration) :

1. Get an estimate $\theta_{m^\star}$ of $\theta_{\tilde{d}}$ over the set of all discretized directions (22) using (28) output :

$$m^\star \text{ such that } \quad |B_{m^\star}| = \max_m |B_m|. \tag{34}$$

2. Using (33), we perform a parabolic fitting of

$$\frac{1}{i}\log(\frac{\hat{\beta}_\ell}{\hat{\beta}_0}e^{-i\ell\theta_{m^\star}}) \simeq \ell\delta\theta + \frac{(\ell^2 - \frac{1}{4})}{2\gamma}. \tag{35}$$

The parabola coefficients are $\delta\theta = \theta_d - \theta_{m^\star}$, the angle correction and the ℓ quadratic term coefficient which depends on the curvature of the front through γ.

3. Correct NMLA amplitudes

$$\{B'_m\} := \mathcal{F}^{-1}(\hat{\beta}_\ell e^{-i(\ell\delta\theta + \frac{(\ell^2-\frac{1}{4})}{2\gamma})}\}), \tag{36}$$

and get the angle corresponding to the maximum of the modulus of the B'_m's. Figure 9 illustrates the improved angle correction.

3.8 Traveltime estimation

We first notice that manual or automatic (most energetic for instance) picking of an event on a seismogram gives an estimate of the traveltime, assuming of course that the source $W_{\omega_s}(t)$ is known. The wavelet is however not a perfect wavefront and may spread over a given period of time (around $.1s$ in our numerical illustration figure 17. NMLA combined with the use of time data can provide an accurate traveltime estimation. The idea is to use the implicit redundancy of the HF traveltime over the frequency range. More precisely we have, again assuming perfect asymptotic one ray ansatz data, and performing the curvature correction of section 3.9 to improve the accuracy :

$$B_{m^\star}(\omega) \simeq A_0 \exp^{i\,\omega\,\phi(x_0)}\,. \tag{37}$$

The ω dependence is explicit in the notation since we are going to use the variation with respect to frequency :

$$\phi(x_0) \simeq \frac{\partial_\omega B_{m^\star}}{i\,B_{m^\star}}. \tag{38}$$

The ω derivative is obtained by applying the same NMLA procedure and post processing to the ω derivative of the data. The derivative data can be computed using finite difference or as we derive the frequency domain from the time domain by computing the Fourier transform of $t\,u(t, x_1, 0)$.

In figure 6, using the case study of section 4.4, we show that this method is more accurate than picking by sliding the center t_0 of a time window around the correct traveltime and plotting the estimated traveltime $\tau = \phi(x_0)$. As long as the time window contains a significant signal the estimated traveltime is constant and correct and therefore does not depend on the picking time as expected.

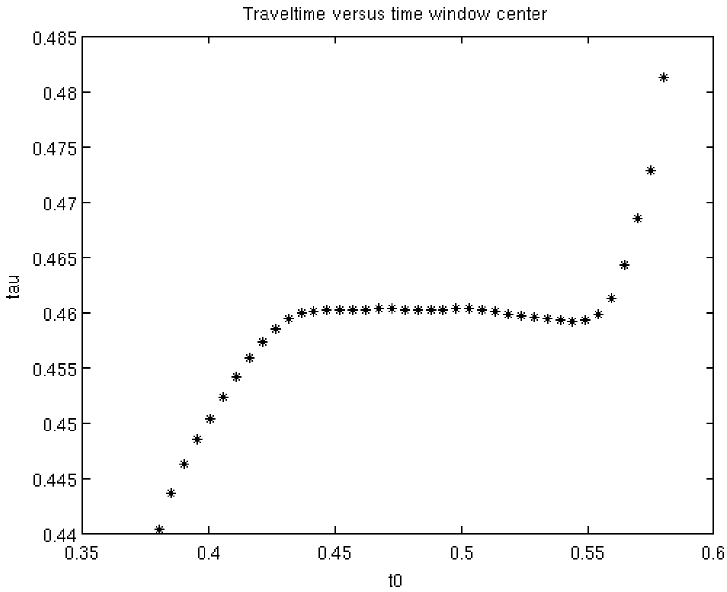

Figure 6: traveltime for different windows

4 Numerical illustration : Source point discovery in Heterogeneous medium

4.1 Generation of synthetic data

We generate synthetic data using the following procedure :

- A standard FDTD scheme (second order in time and space) is used to simulate the time domain propagation from one or more point sources.
- A "Ricker" (Gaussian derivative) is the source wavelet.
- We use a perfect reflecting boundary condition $\frac{\partial}{\partial \nu} u = 0$ at the bottom of the domain and Higher Order Absorbing Conditions, [16], elsewhere.
- We record over time a seismogram (just u) at all discretization points of the domain.
- Once the observation time t_0 and surface position x_0 are picked (see figure 17), a smooth window in space and time can be used to single

out the event.

- We Fourier transform all the time lines, then choose a frequency ω.
- The NMLA frequency data is then computed using the one way method described in appendix A.

4.2 Homogeneous medium

4.3 one source point

Figure 7 depicts the seismogram recorder over time (vertical axis). Each vertical line is the signal $t \to u(t, x)$ recorded at a grid point x on the surface (horizontal axis). The line horizontal deviation is proportional to u thus giving an idea of the succession of waves (events) reaching the surface. In this case there is only one source points but two events due to the reflecting boundary condition at the bottom. Our interface allows to select a time t_0 and a position x_0 (red lines) where we want to perform the NMLA. A window in time can be used to select only one event corresponding to one wavefront and one ray.

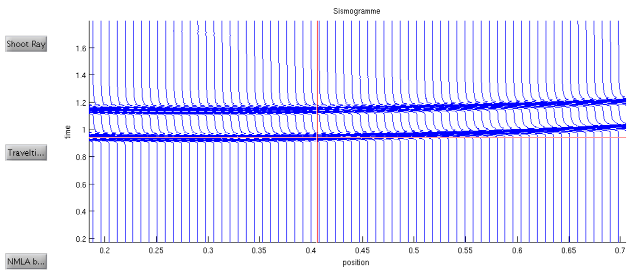

Figure 7: Seismogram and time position picking

Figure 8 shows the impact of α value on the basic NMLA filter (28). If α is too small, we do not have enough Fourier modes to focus, note the angle is still correctly estimated for one ray, however for more than one ray (as in the next section) $\alpha = 10$ would not allow to observe separate maxima when the ray directions are close. If α is too large, then the curvature error induced by the plane wave approximation pollutes the result.

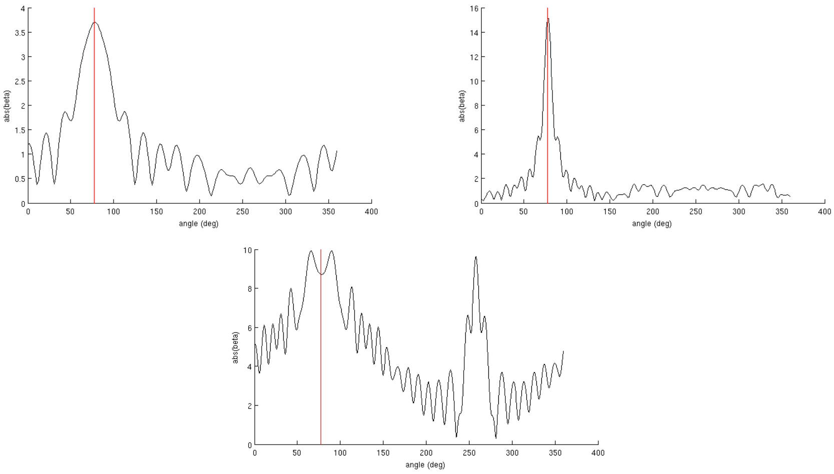

Figure 8: One source point : $|B_m|$ versus θ_m . varying α : 10, 20, 40

Figure 9 shows the output of the NMLA procedure (28) and also the second order correction of section 3.7. After correction the B' amplitudes are better focused around the correct ray angle and the corrected angle is very accurate.

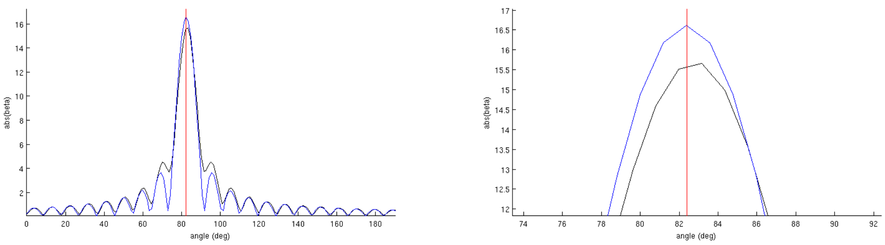

Figure 9: One source point : $|B_m|$ versus θ_m . Left : Black : NMLA - Blue : NMLA + curvature correction - Red vertical line : exact ray direction. Right : Zoom of the max zone.

Table 1 quantifies the error on the angle and the source point discovery. Local Radon transform (LSS) completely fails while NMLA does a better job than plane wave destructor (PWD) (references on these two methods in section 4.6).

Figure 10 shows the error on angle and traveltime when applying NMLA second order to several position on the surface $y = 1$.

Method	Ray angle error	Error (distance to source point)
NMLA basic	0.5988^o	
NMLA 2^{nd} order	0.0184^o	0.0011
LSS	failed	
PWD	0.1917^o	0.0071

Table 1: HF ray direction analysis and source point discovery

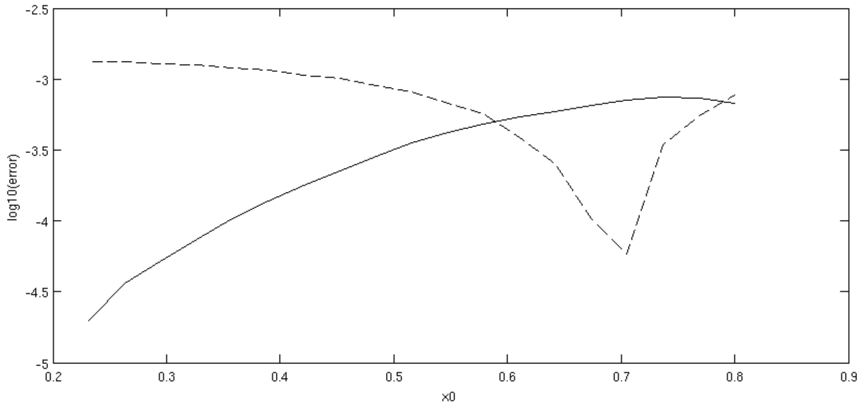

Figure 10: One source point $(0.1, 0.2)$: Angle error (solid line) and Traveltime error (dashed line) versus the position of the observation point x_0 on the "surface" $y = 1$.

4.4 Two source points

Basic NMLA is able to recover well separated multiple rays. We treat here the case of two but it works equally well on more see the original paper [7].

Figure 11 shows the recorded seismogram for two source points. The picked observation point is at equal traveltime from the source points. Thus, the time window will contain two wavefronts and two rays.

Figure 12 shows the NMLA basic filter result on the left and the application of the Gaussian window convolution (45) (see appendix C) which enables to separate the rays if they are not too close and get the $\hat{\beta}$ modes associated to only one ray. Then, the curvature correction and traveltime estimation (section 3.7 and 3.8) can be used.

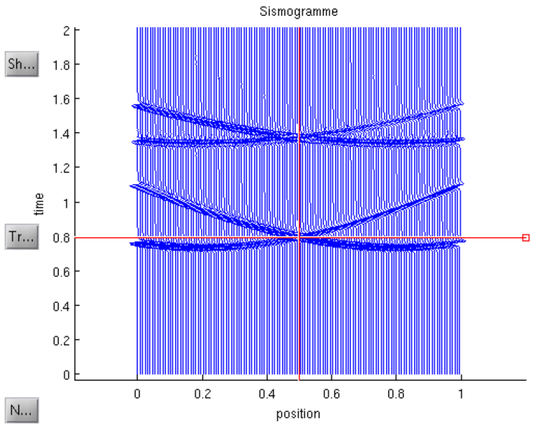

Figure 11: seismogram and time/position picking

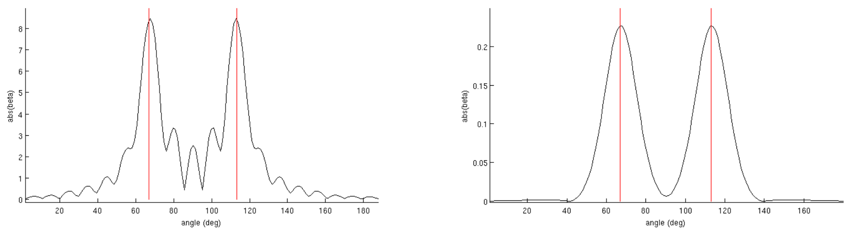

Figure 12: Two source points : $|B_m|$ versus θ_m . Left : Two peaks. Right : Gaussian window to enable separation $a = 2.5$

4.5 Homogeneous medium Noisy data - Stability

These results illustrate the stability claim on the algorithm (section 3.5) for the two source point case. The NMLA filter (28) easily filters out white noise (13) as it is precisely built to single out coherent signals. In order to test correlated noise, we added to the NMLA input data also collected on circle around the observation point but with a different radius, see figure 14.

4.6 Heterogeneous medium one source point

We now consider the smooth speed velocity distribution c of figure 15. The + sign is the source location and our observation point is the cross x at the surface.

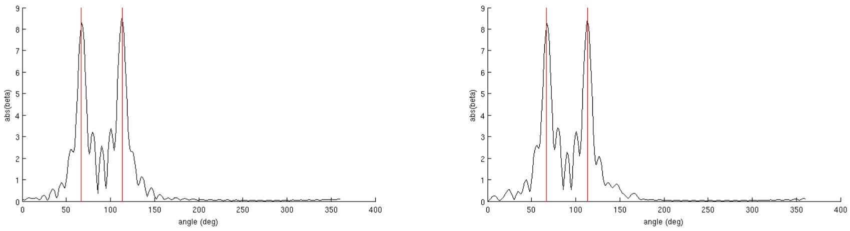

Figure 13: $|B_m|$ versus θ_m . White noise (20%-40%)

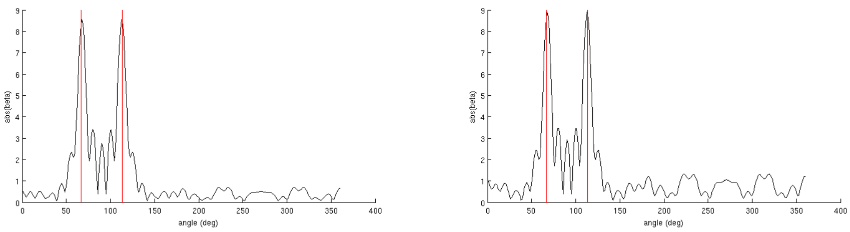

Figure 14: $|B_m|$ versus θ_m . Correlated noise (20%-40%)

Figure 16 shows several snapshots of the FDTD simulation used to generate the synthetic seismogram in figure 17.

Table 2 displays the ray direction found with several methods. NMLA basic and the second order correction. The Plane Wave Destructor Method PWD [23] and the Local Slant Stack LSS (Radon transform) [10] [22] are popular methods in Geophysics and radar processing but are very sensitive to the necessary windowing. Note that PWD is first order by construction; the Radon transform can be generalized to identify parabolas [8] but we did not tested this against NMLA second order. Both PWD and LSS can be considered as image processing methods and do not use at all the wave models.

Figure 18 illustrates the source discovery through the proposed HF TR method (section 2.4) In order to test NMLA performances. NMLA second order yields a $\varphi(x_0) = 0.4602s$. traveltime and we use this together with the different ray directions of table 2 to shoot the rays backwards. Red is NMLA second order, green LSS and yellow PWD. A red circle centered around the actual source position highlight the better performance of NMLA.

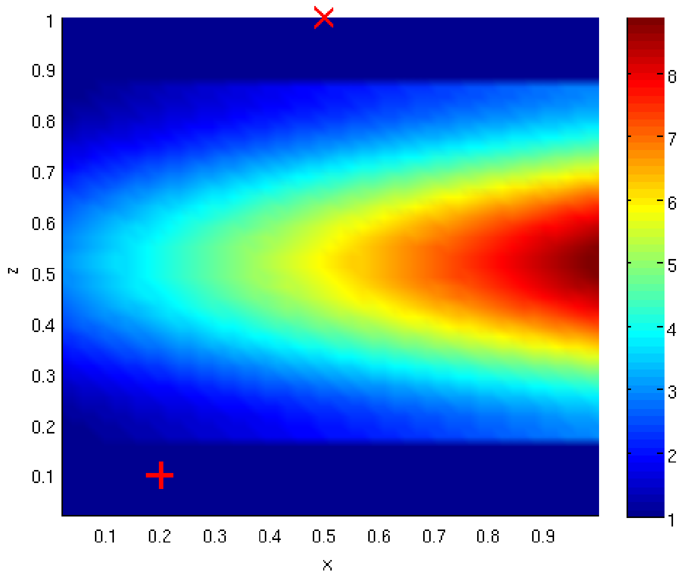

Figure 15: Heterogeneous medium : velocity distribution

5 Conclusion

The new second order version of NMLA method is a robust stable local HF wave analysis tool. Unlike the Plane Wave Destructor, the Local Slant Stack methods (Radon) [10] or other signal procession methods like MUSIC [28], it is based on the true wave HF models and robust even to correlated noise. The companion paper [6] also tries to mathematically establish how close in the near field this method is going to work.

It is completely automatic and has no other tuning parameters than α. A mathematical study of the error depending on α and the discretization parameter M is done in [6]. It also proposes an optimal law for α depending on the front cuvature. The source deconvolution is only needed for the traveltime estimation.

We are confident that NMLA can be extended to 3D and other linear models including elastic waves.

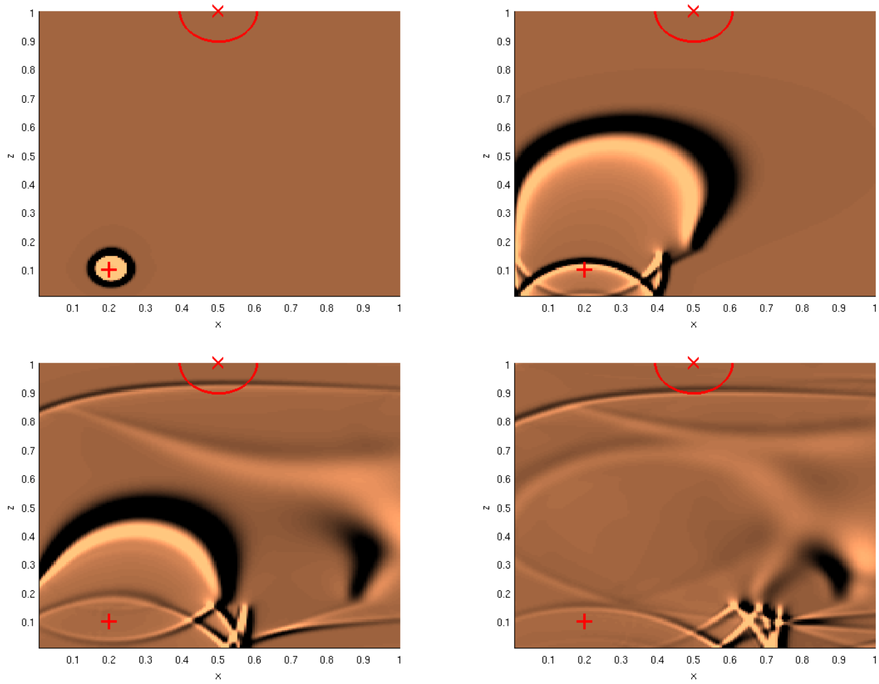

Figure 16: Synthetic data numerical simulation

Potential applications of the method are of course not limited to source point discovery. Here is a non exhaustive list :

- Microlocal finite element methods try to discretize the geometric optic quantities [2] [20]. If known, an analytic solution for the phase ϕ can be use to remove oscillations and the size of the dicretization [14] [26] [24].

- GO is simple and cheap when the underlying wave field is not too complicated (no diffraction, reflections, caustics ...). In these more complicated regime, GO has to manage several complex interacting ansatz. As simple propagating waves can be treated locally by GO, coupling GO and full wave fields across physical interfaces or in a multiscale framework make sense [27] [4] A reliable process to invert the GO ansatz is needed.

- In Geophysics "Cleaning" data by filtering out low frequencies either to use faster HF models of simply because only high frequencies are really

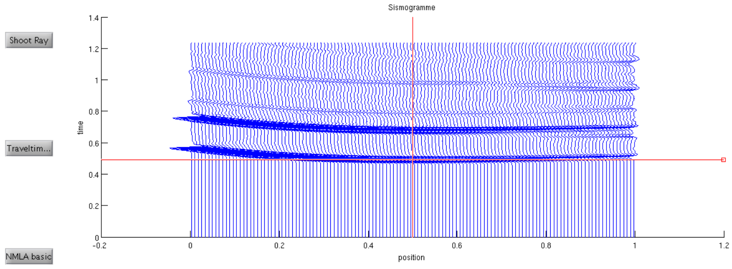

Figure 17: Synthetic seismogram + point/time picking

Method	Ray angle	Error (distance to source point)
NMLA basic	90.2970^o	
NMLA 2^{nd} order	90.5503^o	0.0069
LSS	91.002^o	0.0878
PWD	90.7418^o	0.0201

Table 2: HF ray direction analysis and source point discovery

relevant (migration) or nicer for inversion. (use of Gaussian Beams [29], Curvelets [3], diplets, beamlets ...)

- The Direction of Arrival problem (DOA) is a classic signal processing problem [28] where one tries to find the direction of the source of a signal impinging on a, generally linear, array of antennae
- Source point reduced models for far field representations [11]

It must be stressed that, currently, none of these methods use traveltime nor the amplitude quantities but only the gradient of the traveltime. This seriously hinders their mathematical and numerical development.

Appendix A : Seimogram data/ FT / One-way extrapolation of linear array data

The circular geometry of the observable's support plays an important part in the properties of the K_α operator (26). This is however a constraint for synthetic data as few numerical discretizations of wave fields directly provide

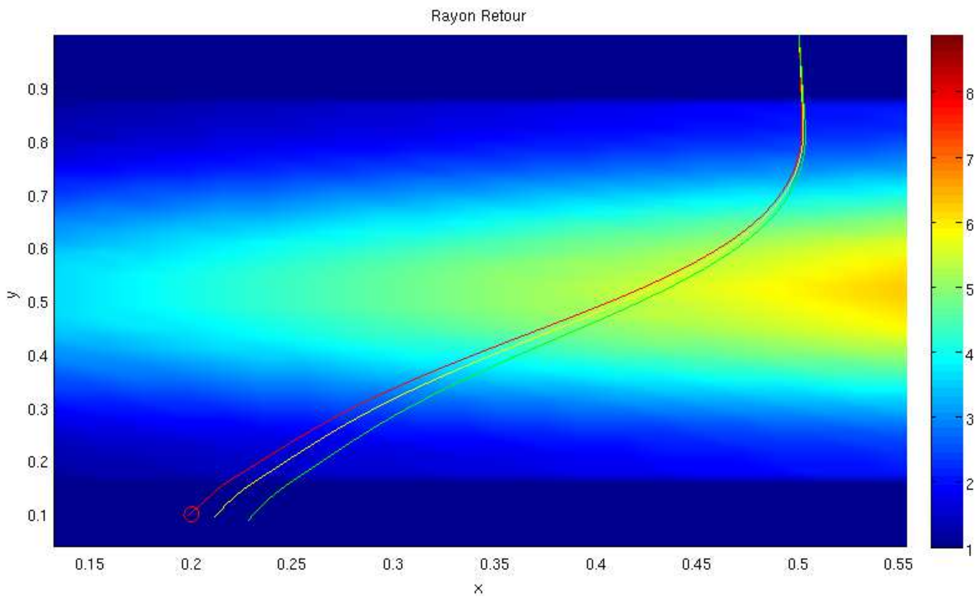

Figure 18: Ray backward propagation with initial conditions specified in table 2.

data on a circular array around an "observation" point. Regarding real data, circular arrays do not seem to be a common acquisition device either. Interpolation is a solution but it needs data on a volume covering the acquisition circle which typically is several wavelengths large.

Considering the most common acquisition format is a linear array, like for instance seismograms recorded on an ideal flat surface in geophysics, we propose here to use one way wave extrapolation to reconstruct the circular array from a seismogram from this type of data .

We assume for simplicity that :

- We are in 2D and $x = (x_1, x_2)$.
- The data $\hat{u}_0(x_1; \omega)$ is given on the surface $x_2 = 1$.
- Our observation point is on the data surface $x_0 = (x_1^o, 1)$.

- The medium speed is constant $c(x) = v$ in a layer containing the observation circle of radius r (see (24)).

We recall here the one way extrapolation procedure. More details, references and also the more complicated case of one way extrapolation in heterogeneous medium, can be found in [17].

First, we Fourier transform the data and Equation (12) with respect to (x_1, x_2) and denote the Fourier space variable (k_1, k_2). Fourier transform rules that the partial derivatives ∂_{x_j} corresponds in Fourier space to a multiplication by, respectively, $-i\, k_j$, that is

$$(k_1^2 + k_2^2 - \frac{\omega^2}{v^2})\, \hat{u}(k_1, k_2; \omega) = 0 \quad \hat{u}_0(k_1; \omega) \text{ given on } x_2 = 1. \tag{39}$$

We keep the $\hat{u}$ notation and drop the ω dependence for simplicity. If we restrict ourselves to real "up-going" $k_2 > 0$ Fourier mode, *this is the one way assumption*, and after factorization, equation (39) can be simplified into

$$(k_2 - \sqrt{\frac{\omega^2}{c^2} - k_1^2})\, \hat{u}(k_1, k_2) = 0. \tag{40}$$

The significant real Fourier modes of the solutions have to satisfy the (so called) "dispersion" relation characterizing the paraxial operator :

$$k_2 = \sqrt{\frac{\omega^2}{c^2} - k_1^2}. \tag{41}$$

The solution can be computed as a function of (k_1, x_2). Indeed after an inverse Fourier transform in x_2, we get the ODE (we abusively keep the $\hat{u}$ notation again)

$$-i\partial_{x_2}\hat{u}(k_1, x_2) = k_2\hat{u}(k_1, x_2) \quad \hat{u}(k_1, 1) = \hat{u}_0(k_1), \tag{42}$$

where k_2 is given by (41), with trivial solution The exact solution of (42) at depth x_2 is

$$\hat{u}(k_1, x_2) = \hat{u}_0(\omega, k_1)\, e^{i\, k_2\, x_2}.$$

The solution at any point (x_1, x_2) is recovered by inverse Fourier transform from k_1 to x_1.

This procedure generates the data on a circular array for up-going rays in constant medium at the price of two 1D Fourier transforms. It could also be used to filter out down-going rays. As we restrict to observation point near the $x_2 = 1$ depth of the linear array, it is possible to use a x_1 windows which size depends on the finite speed v and the resulting dependence cone.

Appendix B : When the wavelet W_{ω_s} is unknown

In that case, the source deconvolution (18) is not possible so we just remove the half primitive factor

$$\hat{u}(x;\omega) \leftarrow \sqrt{-i\omega}\,\hat{u}(x,\omega). \tag{43}$$

This implies that the NMLA algorithm expected output is multiplied by the frequency domain wavelet

$$B \leftarrow B\hat{W}_{\omega_s}(\omega). \tag{44}$$

The curvature correction method of section 3.8 is unchanged since the amplitudes are removed in (35).

The traveltime estimation method (38) does not work since the amplitude $B_{m^\star}$ contains now the wavelet with an unknown ω dependant phase.

Appendix C :Time and direction windows

As shown in Figure 17 we assume that, after picking the observation point $x_0 = (x_1^0, 1)$ on the surface data (the vertical red line), we select an observation time in the seismogram (the horizontal red line). This can be done by the user or an *ad hoc* automatic signal processing procedure.

The advantage of time picking, is that rays crossing at the observation point with different traveltime may be separated using a time window. In Figure 17 we see that a second later wavefront passes the observation point. If we just Fourier transform in time and then perform NMLA, we expect β_α to correspond a two ray ansatz. Conversely, using a smooth time window,

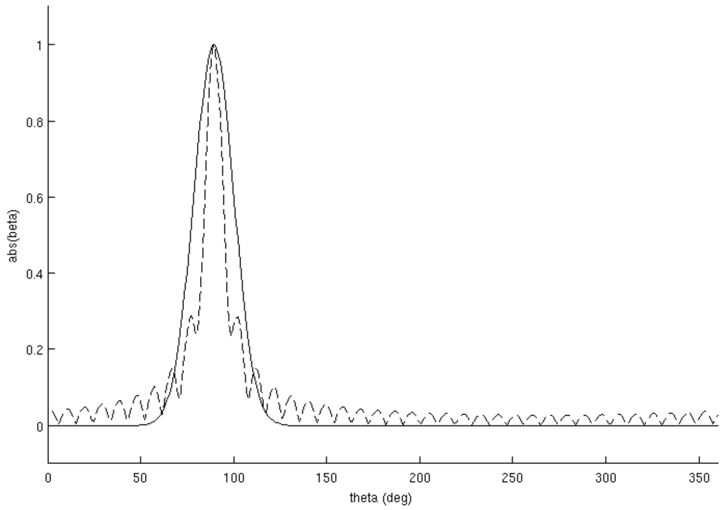

Figure 19: Solid line incorporates Gaussian window. One source point.

we are able to select for instance only the first arrival. In this case we only have one ray and can perform the curvature correction on section 4.

The oscillations of S_α produced by the truncation of the harmonic series may be a problem to identify the maxima of the B's. To avoid these small spurious oscillations, or to avoid them being mixed with noise, it is possible to convolute B with a smooth Gaussian weight function for instance. This is simply done using a additional filter in Fourier space before the last Fourier transform in (28) :

$$\hat{\beta}_\ell \leftarrow \hat{\beta}_\ell \hat{w}_\ell \quad \{\hat{w}_\ell\} = \mathcal{F}(\{\exp^{\frac{a}{2}\theta_m^2}\}) \tag{45}$$

where a can be used to tune the Gaussian filter. Figure (19) shows comparison for one source point in homogeneous medium. See also figure 12.

References

[1] *Partial differential equations. V*, volume 34 of *Encyclopaedia of Mathematical Sciences*. Springer-Verlag, Berlin, 1999. Asymptotic methods for partial differential equations, A translation of ıt Current prob-

lems in mathematics. Fundamental directions. Vol. 34 (Russian), Akad. Nauk SSSR, Vsesoyuz. Inst. Nauchn. i Tekhn. Inform., Moscow, 1988 [MR1066954 (91e:35002)], Translation by J. S. Joel and S. A. Wolf, Translation edited by M. V. Fedoryuk.

[2] T. Abboud, J.-C. Nédélec, and B. Zhou. Méthode des équations intégrales pour les hautes fréquences. *C. R. Acad. Sci. Paris Sér. I Math.*, 318(2):165–170, 1994.

[3] H. B. Sun, Chauris and J. Ma. 3d post-stack one-way migration using curvelets. *Journal of Seismic Exploration, submitted*, 2010.

[4] M. Balabane and V. Tirel. Décomposition de domaine pour un calcul hybride de l'équation de Helmholtz. *C. R. Acad. Sci. Paris Sér. I Math.*, 324(3):281–286, 1997.

[5] J.-D. Benamou. An introduction to Eulerian geometrical optics (1992-2002). *SIAM J. Sci. Comp.*, 2002. To appear.

[6] Jean-David Benamou, Francis Collino, and Simon Marmorat. Second order stable numerical microlocal analysis of harmonic plane wave and source point wavefields. *submitted*, 2011.

[7] Jean-David Benamou, Francis Collino, and Olof Runborg. Numerical microlocal analysis of harmonic wavefields. *J. Comput. Phys.*, 199(2):717–741, 2004.

[8] Gregory Beylkin. Discrete Radon transform. *IEEE Trans. Acoust. Speech Signal Process.*, 35(2):162–172, 1987.

[9] Liliana Borcea, George Papanicolaou, and Chrysoula Tsogka. Theory and applications of time reversal and interferometric imaging. *Inverse Problems*, 19(6):S139–S164, 2003. Special section on imaging.

[10] B. Borden and M. Cheney. Microlocal isar for low signal-to-noise environments. In *Proceedings of the Radar, 2006 IEEE Conference*, 2006.

[11] Brett Borden. Radar scattering centre localization by subspace fitting. *Inverse Problems*, 17(5):1483–1491, 2001.

[12] Q. Carayol and F. Collino. Error estimates in the fast multipole method for scattering problems. II. Truncation of the Gegenbauer series. *M2AN Math. Model. Numer. Anal.*, 39(1):183–221, 2005.

[13] Quentin Carayol and Francis Collino. Error estimates in the fast multipole method for scattering problems. I. Truncation of the Jacobi-Anger series. *M2AN Math. Model. Numer. Anal.*, 38(2):371–394, 2004.

[14] S. N. Chandler-Wilde, S. Langdon, and L. Ritter. A high-wavenumber boundary-element method for an acoustic scattering problem. *Philos. Trans. R. Soc. Lond. Ser. A Math. Phys. Eng. Sci.*, 362(1816):647–671, 2004.

[15] Didier Cassereau Claire Prada, Estelle Kerbrat and Mathias Fink. Time reversal techniques in ultrasonic nondestructive testing of scattering media. *Inverse Problems*, 18, 2002.

[16] F. Collino. Conditions aux limites absorbantes d'ordre élevé pour les modèles de propagation d'onde. problème des domaines rectangulaires. Technical Report 1790, INRIA., Domaine de Voluceau, Rocquencourt, France, 1992.

[17] F. Collino and B. Lavaud. Peut-on obtenir des amplitudes correctes avec les quations paraxiales ? Technical Report 3004, INRIA., Domaine de Voluceau, Rocquencourt, France, 1996.

[18] F. Collino and Marmorat S. Analyse microlocale dans le domaine temporel. Technical report, INRIA., Domaine de Voluceau, Rocquencourt, France, 2010.

[19] D. Colton and R. Kress. *Inverse Acoustic and Electromagnetic Scattering Theory*, volume 93. Springer-Verlag, 1992.

[20] A. de la Bourdonnaye and M. Tolentino. Numerical simulation of scattering problems with Fourier-integral operators. *Math. Models Methods Appl. Sci.*, 7(5):613–631, 1997.

[21] B. Engquist and O. Runborg. Computational high frequency wave propagation. *Acta Numerica*, 12, 2003.

[22] Hugonnet et al. High resolution radon: a review. In *Proceedings of the EAGE 63 rd Conference and Technical Exhibition*, Amsterdam, The Netherlands, June 2001.

[23] S. Fomel. Applications of plane-wave destructor filters:. Technical Report 105, SEP, 2000.

[24] E. Giladi and J. B. Keller. A hybrid numerical asymptotic method for scattering problems. *J. Comput. Phys.*, 174(1):226–247, 2001.

[25] Y. Landa, Nicolay M. Tanushev, and Tsai R. Discovery if point sources in the hemlhotz equation posed in unknown domains with obstacle. 2010.

[26] S. Langdon, M. Mokgolele, and S. N. Chandler-Wilde. High frequency scattering by convex curvilinear polygons. *J. Comput. Appl. Math.*, 234(6):2020–2026, 2010.

[27] L. N. Medgyesi-Mitschang and D.-S. Wang. Hybrid methods for analysis of complex scatterers. *P. IEEE*, 77(5):770–779, 1989.

[28] B. Porat and B. Friedlander. Analysis of the asymptotic relative efficiency of music algorithm. *IEEE Trans. Acoust., Speech Signal Process.*, 36(4):532–544, 1988.

[29] Nicolay M. Tanushev, Björn Engquist, and Richard Tsai. Gaussian beam decomposition of high frequency wave fields. *J. Comput. Phys.*, 228(23):8856–8871, 2009.

[30] William Hodgkiss W. Kuperman and Hee Song. Phase conjugation in the ocean: Experimental demonstration of an acoustic time-reversal mirror. *Journal of the Acoustical Society of America*, 103, 1998.

[31] G. N. Watson. *A treatise on the theory of Bessel functions*. Cambridge University Press, 1966.

Centre de recherche INRIA Paris – Rocquencourt
Domaine de Voluceau - Rocquencourt - BP 105 - 78153 Le Chesnay Cedex (France)

Centre de recherche INRIA Bordeaux – Sud Ouest : Domaine Universitaire - 351, cours de la Libération - 33405 Talence Cedex
Centre de recherche INRIA Grenoble – Rhône-Alpes : 655, avenue de l'Europe - 38334 Montbonnot Saint-Ismier
Centre de recherche INRIA Lille – Nord Europe : Parc Scientifique de la Haute Borne - 40, avenue Halley - 59650 Villeneuve d'Ascq
Centre de recherche INRIA Nancy – Grand Est : LORIA, Technopôle de Nancy-Brabois - Campus scientifique
615, rue du Jardin Botanique - BP 101 - 54602 Villers-lès-Nancy Cedex
Centre de recherche INRIA Rennes – Bretagne Atlantique : IRISA, Campus universitaire de Beaulieu - 35042 Rennes Cedex
Centre de recherche INRIA Saclay – Île-de-France : Parc Orsay Université - ZAC des Vignes : 4, rue Jacques Monod - 91893 Orsay Cedex
Centre de recherche INRIA Sophia Antipolis – Méditerranée : 2004, route des Lucioles - BP 93 - 06902 Sophia Antipolis Cedex

Éditeur
INRIA - Domaine de Voluceau - Rocquencourt, BP 105 - 78153 Le Chesnay Cedex (France)
http://www.inria.fr
ISSN 0249-6399